NASA CONTRACTOR REPORT

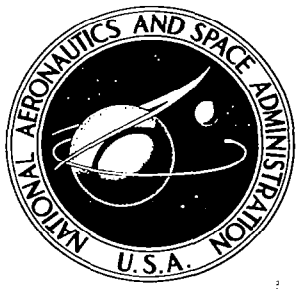

NASA CR-590

TRANSISTOR DESIGN EFFECTS ON RADIATION RESISTANCE

by V. R. Honnold, G. D. Thomas, and C. C. Berggren

Prepared by
HUGHES AIRCRAFT COMPANY
Fullerton, Calif.
for Langley Research Center

NATIONAL AERONAUTICS AND SPACE ADMINISTRATION • WASHINGTON, D. C. • SEPTEMBER 1966

NASA CR-590

TRANSISTOR DESIGN EFFECTS ON RADIATION RESISTANCE

By V. R. Honnold, G. D. Thomas, and C. C. Berggren

Prepared under Contract No. NAS 1-4595 by
HUGHES AIRCRAFT COMPANY
Fullerton, Calif.

for Langley Research Center

NATIONAL AERONAUTICS AND SPACE ADMINISTRATION

For sale by the Clearinghouse for Federal Scientific and Technical Information
Springfield, Virginia 22151 – Price $2.50

TABLE OF CONTENTS

LIST OF FIGURES

LIST OF TABLES

1.0 INTRODUCTION

The degrading effect of high energy space radiation on semiconductors is well recognized. The present program investigates the problem of minimizing this effect in a particular semiconductor device. A double diffused silicon planar transistor, the 2N708, was chosen for the investigation since it is representative of a class of high frequency, multipurpose transistors which are in general use. In addition to the 2N708 study, the radiation response of a majority carrier device - a multichannel field effect transistor intended for high frequency, high power application - was also investigated.

The work consisted of a theoretical and an experimental phase. The former investigated the influence of surface recombination and geometrical factors on DC current gain utilizing a cylindrical model for the planar configuration. The results of experiment indicated the presence of high level injection effects, and the theory was extended accordingly. The experimental program consisted of several phases. The first was a fabrication phase. Concurrent with device fabrication was the development of instrumentation for data acquisition. The importance of determining device degradation for a range of operating points, together with the number of variations, dictated that the acquisition be automated. An automatic data acquisition system was developed to record degradation automatically in a form compatible with its reduction and print out by digital computer.

Device irradiations were carried out with both electrons and protons. The former at two energies, 1 and 8 Mev, and the latter at 31 Mev utilizing the University of Southern California proton linear accelerator. In all, six separate electron and proton irradiations were performed in intercomparing design variations and in a final comparison of a radiation resistant prototype design with off-the-shelf units from other manufacturers.

The DC common base current gain, α, was selected as the standard of comparison in all cases. It was measured directly as a voltage drop in the collector circuit, at constant emitter current, as a function of time integrated particle flux. The following design variations were significant for radiation resistance, (a) small emitter area, (b) heavy emitter doping, (c) small base width, (d) gold doped collector, (e) Czochralski material. In addition to these results, the experiments showed a further important dependence of degradation rate on injection level, or operating point. In particular, the rate decreases with increasing injection level.

The above results were preliminary to the primary objectives of the present investigation of (a) demonstrating that these desirable variations could be incorporated into a radiation resistant prototype 2N708, and (b) of developing analytical expressions that correlated the experimental results and that furnished the basis for further design studies. Both objectives were met. The prototype transistor in tests with 31 Mev protons, and in comparison with three devices of other manufacture, showed the smallest degradation rate. The prototype was within design specifications in all but common emitter current gain and $V_{CE(SAT)}$. In the case of the second objective, the underlying physical phenomenon was found in the presence of effects dependent upon the level of minority carriers injected into the base.

2.0 THEORETICAL MODEL DEVELOPMENT

2.1 The Cylindrical Transistor Model

In a design effects investigation, two general directions are possible at the outset in developing a transistor model. In the first, current flow is assumed to occur under conditions of low level injection and the effects produced by a lack of uniformity in the current flow are of interest. This lack of uniformity occurs because of the presence of surface recombination, for example, or because of the actual finite size of the emitter and collector. In the second, effects that occur under conditions of high level injection, or that result from a nonuniform doping profile, or both, are of primary interest. Generally, when these latter types of effects are under consideration, uniform or one-dimensional current flow is assumed for simplicity. The present investigation begins with the first line of development. A cylindrical model[1] for the transistor is adopted with surface recombination included in the emitter plane. The treatment is then extended in the next Section to include the effects of high level injection.

The configuration for the cylindrical model is shown in Figure (2-1). The emitter radius is r_e, and for $r > r_e$ the surface is characterized by a surface recombination velocity s. The emitter is assumed to have negligible thickness, the base width is W, and the collector plane at $z = W$ is assumed infinite in extent, and a sink for minority carriers. The minority carrier density in the base region, $q(r, z)$ for the case of cylindrical symmetry about the z-axis, obeys the following equation,

$$\left[1/r\ (\partial/\partial r)\ \ (r\ \partial/\partial r) + \partial^2/\partial z^2 - 1/L^2\right]\ q(r,z) = 0 \qquad (2.1)$$

where L is the minority carrier diffusion length in the base. The boundary conditions are as follows,

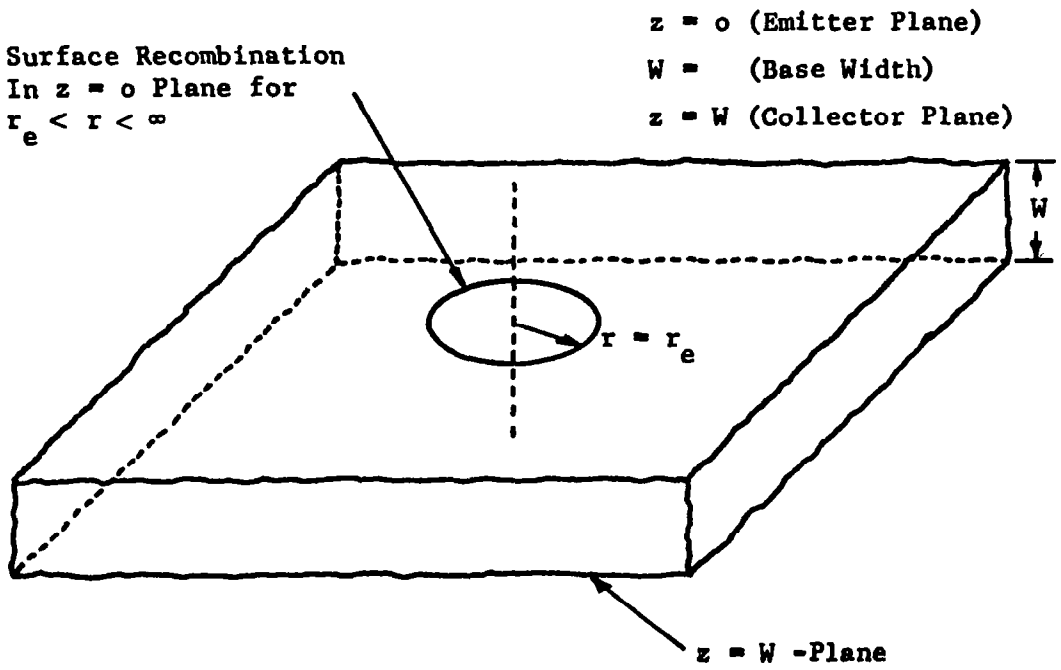

FIGURE 2-1 Cylindrical Transistor Model

$$q(r,0) = q_e \; ; \qquad 0 \leq r < r_e \; , \tag{2.2}$$

$$(\partial/\partial z - s/D)q = 0 \; ; \qquad z = 0, \; r_e < r < \infty \; , \tag{2.3}$$

$$q(r,W) = 0 \; ; \qquad 0 \leq r < \infty \; , \tag{2.4}$$

Define the Hankel transform, $\varphi(p,z)$, of $q(r,z)$ as follows,

$$\varphi(p,z) = \int_0^\infty q(r,z) r J_o(rp) dr \tag{2.5}$$

This transform applied to Equation (2.1) yields the ordinary differential equation,

$$\left[d^2/dz^2 - (p^2 + k^2) \right] \varphi(p,z) = 0 \; , \qquad k = L^{-1} \; . \tag{2.6}$$

The general solution of Equation (2.6) is given by,

$$\varphi(p,z) = \varphi_1(p) \; e^{\gamma z} + \varphi_2(p) \; e^{-\gamma z} \; , \tag{2.7}$$

where $\gamma^2 = p^2 + k^2$ and where φ_1 and φ_2 are functions of p that will be determined by the boundary conditions given in Equations (2.2), (2.3), and (2.4). The unknown charge density $q(r,z)$ is expressed in terms of $\varphi(p,z)$ by the inversion theorem for the Hankel transform,

$$q(r,z) = \int_\delta^\infty \varphi(p,z) p J_o(rp) dp \tag{2.8}$$

Equation (2.8) is next combined with Equation (2.7) to give,

$$q(r,z) = \int_0^\infty pJ_o(rp) \left[\varphi_1 e^{\gamma z} + \varphi_2 e^{-\gamma z}\right] dp \qquad (2.9)$$

In accordance with the boundary conditions, we have from Equation (2.9), the following,

$$q(r,0) = \int_0^\infty pJ_o(rp) \left[\varphi_1 + \varphi_2\right] dp = q_e \ , \ 0 \leq r < r_e, \qquad (2.10)$$

$$(\partial/\partial z - s/D)\ q\ (r,z)\ \Big|_{z=0} = \int_0^\infty pJ_o(rp) \left[(\gamma - s/D)\varphi_1 - (\gamma + s/D)\varphi_2\right] dp = 0,$$

$$r_e < r < \infty, \qquad (2.11)$$

$$q(r,W) = \int_0^\infty pJ_o(rp) \left[\varphi_1 e^{\gamma W} + \varphi_2 e^{-\gamma W}\right] dp = 0 \ , \ 0 \leq r < \infty. \qquad (2.12)$$

From Equation (2.12) we have

$$\varphi_1 = -\varphi_2 e^{-2\gamma W} \qquad (2.13)$$

If a new function, $\varphi(p)$ is defined as follows,

$$\varphi(p) = p\varphi_2 \left[\gamma W\ (1 + e^{-2\gamma W}) + \lambda(1 - e^{-2\gamma W})\right] \ , \qquad (2.14)$$

where $\lambda = sW/D$, then Equations (2.10) and (2.11) reduce to,

$$\int_0^\infty \varphi(p)\ J_o(rp) \left[\tanh\gamma W/(\gamma W + \lambda \tanh\gamma W)\right] dp = q_e \ , \ 0 \leq r < r_e \ , \qquad (2.15)$$

and

$$\int_0^\infty \varphi(p)\ J_o(rp)\, dp = 0 \ , \ r_e < r < \infty \qquad (2.16)$$

A solution to the dual integral Equations (2.15) and (2.16) leads to an explicit expression for $\varphi(p)$, which, through Equations (2.14), (2.13), and (2.7), in turn leads to the function, $\varphi(p,z)$ defined by Equation (2.7). The desired minority carrier charge density expression then follows from Equation (2.8),

$$q(r,z) = \int_0^\infty \varphi(p,z)\ pJ_o(rp)dp \tag{2.8}$$

It is shown in the Appendix that for the special case of zero surface recombination velocity, the density $q(r,z)$ is given by,

$$q(r,z) = r_e q_e \left[(W/L)/\tanh(W/L)\right] \int_0^\infty \left[\sinh\gamma(W-z)/(\gamma W\cosh\gamma W)\right] J_1(r_e p)J_o(rp)dp \tag{2.17}$$

in the limit, $(W/r_e) << 1$.

The emitter and collector currents then follow from Equation (2.17) in accordance with the following expressions,

$$I_E = 2\pi\epsilon D \int_0^{r_e} (\partial q(r,z)/\partial z)_{z=0}\ rdr \tag{2.18}$$

$$I_C = 2\pi\epsilon D \int_0^\infty (\partial q(r,z)/\partial z)_{z=W}\ rdr \quad , \tag{2.19}$$

where ϵ is the electronic charge. The common base current gain, α, then follows directly from Equations (2.18) and (2.19) in accordance with the definition,

$$\alpha = I_C/I_E = \text{sech}\ (W/L), \quad (W/r_e) << 1, \tag{2.20}$$

where majority carrier flow is neglected.

In the limit, then, for the base width small compared to the emitter radius, which is a good approximation for the planar configuration under consideration, the current gain α is given by Equation (2.20). With the assumption, which is also good for the present device, that the base width is small compared to the diffusion length L, α becomes,

$$\alpha \cong 1 - 1/2\ (W/L)^2 \quad , \tag{2.21}$$

which is in agreement with the result obtained from the case of flow in one dimension.

Equation (2.21) is deficient in the sense that it has been obtained with the neglect of surface recombination. It is important to establish the relative importance of surface recombination for the present design study and, accordingly, the more general result for the case of a nonzero surface recombination velocity was obtained. The solution, based on Equations (2.15) and (2.16) derived above, is an extension of that presented in the Appendix. With $\lambda(=sW/D) \neq 0$ it is given by,

$$\alpha \cong \text{sech}\ (W/L) \left[1 + 2\ (2/\pi)^3\ (sW^2/Dr_e)\right]^{-1} \quad , \tag{2.22}$$

with the approximation $(sW/D) \ll 1$. For the case of zero s, the solution for α reduces to that given previously in Equation (2.20). The value of the parameter, λ for some typical values is,

$$\lambda = sW/D = (10^3\ \text{cm/sec})\ (10^{-4}\ \text{cm})/(38\ \text{cm}^2/\text{sec}) \cong 3 \times 10^{-3} \ .$$

With the previous assumption that $(W/r_e) < < 1$, the last term in brackets in Equation (2.22) is small compared to one and the

bracketed expression may be expanded as follows,

$$\alpha \cong \text{sech } (W/L) \left[1 - 2(2/\pi)^3 \ (sW^2/Dr_e) + \cdots\right] , \qquad (2.23)$$

$$\cong 1 - 1/2(W/L)^2 - 2 \ (2/\pi)^3 \ (sW^2/Dr_e) , \qquad (2.24)$$

if, as before, $(W/L) << 1$. Equation (2.24) may be compared with Equation (2.21); the effect of a finite surface recombination velocity is evident in the third term and appears as a correction to the previous result for zero surface recombination. The magnitude of this term may be estimated for the planar device under consideration,

$$sW^2/Dr_e = (sW/D) \ (W/r_e) \cong (3 \times 10^{-3}) \ (10^{-4}/3 \times 10^{-3}) \cong 10^{-4}$$

for a 2 mil diameter emitter. This estimate is based on an assumed value of 10^3 cm/sec for the surface recombination velocity. It is difficult to determine an exact value for s; 10^3 cm/sec probably represents an upper limit.

It may be concluded, therefore, that the predominant term affecting, α; for the present model in which majority carrier effects are neglected, that is, unit emitter efficiency and low level injection; is the term,

$$\alpha \cong 1 - 1/2 \ (W/L)^2 = \beta^* , \qquad (2.25)$$

where β^* designates the base transport factor. This result is the same as would result from a one-dimensional current flow analysis; it has been derived here as a limiting case of a more accurate representation of the distribution of minority carrier charge density in the transistor base region. In this way an

accurate determination has been made of the relative importance of volume versus surface effects.

2.2 High Level Injection Effects

The previous Section was concerned with the effects of geometry and with the relative importance of surface and volume in determining a more accurate representation of the transistor. In order to make this problem tractable, it was necessary to make the following simplifications: (a) low level injection, (b) unit emitter efficiency, and (c) zero impurity gradient. It will be shown subsequently from the experimental data that injection level effects are of particular importance. The present Section, therefore, will generalize the results of the previous one by taking into account injection level effects on the transistor current gain.

Expressions for the common emitter current gain, taking into account injection level effects, have been developed by Rittner,[2] Messenger and Spratt,[3] Phillips,[4] and by Messenger;[5] the latter author has also pointed out a lack of accuracy in Webster's[6] original treatment of the subject.

The level of injected carriers in the base region of the transistor affects the current gain in two ways. In the first, the presence of increasing numbers of minority carriers in the base requires additional majority carriers in order to maintain electrical neutrality. In the case of the n-p-n device, the hole density in the base must increase to compensate for an increase in the number of electrons injected into the base from the emitter. The second effect that occurs is due to a change in the minority carrier lifetime with increasing injection level.

Both of these effects will modify the base current amplitude and with it the current gain as the number of minority carriers

injected into the base increases. The current gain under these circumstances can be computed as follows. With the assumption of negligible surface recombination and unity emitter injection efficiency, the base current will be that required for volume recombination. It will be given by the expression, [2]

$$I_{vB} = qAW \left[(n-n_o)/\tau\right]_{Av} \tag{2.26}$$

where τ is the minority carrier lifetime in the base, n_o the thermal equilibrium density, A is the emitter area, W is the base width, and q is the electronic charge. The average that is indicated is a volume average taken over the base volume,

$$\left[(n-n_o)/\tau\right]_{Av} = (1/AW)\iiint_{Base}\left[(n-n_o)/\tau\right] dxdydz$$

$$= (1/W)\int_o^W \left[(n-n_o)/\tau\right] dz. \tag{2.27}$$

The second form of Equation (2.27) follows with the simplifying assumption that the current is one dimensional in the z-direction. To a first approximation with only a small amount of recombination, the distribution of minority carries in the base region will be nearly linear,

$$n(z) = n_E(1-z/W), \tag{2.28}$$

where n_E is the injected electron density at the base edge of the emitter base junction (z=0); n_E will be determined by the injection level; the ratio (n_E/N_a), where N_a is the acceptor doping level in the p-type base, may be referred to as an injection level parameter. Low level injection occurs for $(n_E/N_a) << 1$, high level for the case $(n_E/N_a) \geq 1$. The minority carrier

lifetime, τ, in the base region, according to the theory of recombination of Shockley and Read,[7] will be given, for an arbitrary injection level, by the expression,

$$\tau(n) = \tau_o \left[1 + a(n-n_o) \right] / \left[1 + c(n-n_o) \right] \quad , \tag{2.29}$$

where τ_o is the low level lifetime, and the constants "a" and "c", in accordance with the theory, are defined by the general expressions,

$$a = \left[\tau_{po} + \tau_{no} \right] / \left[\tau_{po} \, (n_o + n_1) + \tau_{no} \, (p_o + p_1) \right] \quad , \tag{2.30}$$

$$c = (n_o + p_o)^{-1} \quad . \tag{2.31}$$

Equations (2.28) and (2.29) may now be substituted into Equation (2.27); for $n_E >> n_o$,

$$\left[(n-n_o)/\tau \right]_{Av} = (1/W) \int_o^W \frac{n_E(1-z/W)}{\tau_o} \left[1+cn_E \, (1-z/W) \right] \left[1+an_E(1-z/W) \right]^{-1} dz \tag{2.32}$$

When the result of the integration is substituted into Equation (2.26), the following expression results,

$$I_{vB} = (qAn_E W/\tau_o) \left\{ (1/an_E)+(c/2a)-(c/a^2 n_E)+(1/a^2 n_E^2) \left[(c/a) -1 \right] \log_e (1+an_E) \right\}$$

$$= (qAn_E W/\tau_o) \, F \quad , \tag{2.33}$$

where F stands for the factor in braces.

In order to compute the desired current gain expression, an equation for the emitter current is also required. It can be shown[4] that under high level injection conditions, it is given by,

$$I_{nE} = (qAD_n n_E/W)\left[(N_a+2n_E)/(N_a+n_E)\right] \tag{2.34}$$

The base transport factor, β^*, introduced in Equation (2.25) may now be generalized to take into account high level injection effects. According to its definition, β^*, represents that fraction of the injected minority carriers that reach the collector, the rest are lost to volume recombination in the base. Therefore,

$$\alpha = \beta^* = 1 - (I_{vB} / I_{nE}) \tag{2.35}$$

With the substitutions of Equations (2.33) and (2.34) into (2.35), the following expression results for the current gain,

$$\alpha = \beta^* = 1-(W^2/D\tau_o)\ F\ \ (1+n_E/N_a)/(1+2n_E/N_a) \tag{2.36}$$

Equation (2.36) represents the current gain corrected for high level injection. It may be compared to Equation (2.25) which is the low level expression. Equation (2.36) will now be rewritten in a more specific form applicable to the p-type base region of the planar transistor under study. For this case the Shockley-Read constants "a" and "c" defined in Equations (2.30) and (2.31) become,

$$a \cong (\tau_{po} + \tau_{no})/\tau_{no}p_o \cong \tau_\infty /\tau_{no}N_a\ ;\quad \tau_{no} \equiv \tau_o\ , \tag{2.37}$$

$$c \cong p_o^{-1} = N_a^{-1} \tag{2.38}$$

where τ_∞, as defined by Shockley and Read, is the limiting lifetime reached at infinitly large injection levels. With the introduction of the relations given in Equation (2.37) into the factor F expression given in Equation (2.33), F will be a function of the dimensionless parameters (n_E/N_a) and (τ_o/τ_∞). To a good approximation [4] (n_E/N_a) can be replaced by a factor $(Z/2)$, where Z is an injection level parameter first introduced by Webster[6] in his treatment of the variation of current gain with injection level. It is defined by,

$$Z = I_{nE}W/qADN_a \tag{2.39}$$

The introduction of this parameter into the current gain expression is of particular importance for the present investigation because it represents the following design variations, the base width W, the emitter area A, and the base doping level N_a.

In addition, the emitter current I_{nE} which is an experimental variable also appears. With the introduction of Z and the relations expressed by Equations (2.37) and (2.38) into Equation (2.36), the common base current gain α becomes,

$$\alpha\left[Z,(\tau_o/\tau_\infty)\right] = 1-(W^2/L^2)F\left[Z,(\tau_o/\tau_\infty)\right]\left[(1+Z/2)/(1+Z)\right] \tag{2.40}$$

where the explicit dependence of α on the parameters Z and (τ_o/τ_∞) is indicated. The factor F is given by the expression,

$$F\left[Z,(\tau_o/\tau_\infty)\right] = (\tau_o/\tau_\infty)(2/Z)+(1/2)(\tau_o/\tau_\infty)-(\tau_o/\tau_\infty)^2(2/Z)+(\tau_o/\tau_\infty)^2$$
$$(2/Z)^2\left((\tau_o/\tau_\infty)-1\right)\log_e\left(1+(\tau_\infty/\tau_o)(Z/2)\right)$$

In the limit of small injection level,

$$F\left(Z,(\tau_o/\tau_\infty)\right) \sim 1/2,$$

and agreement is obtained with the previous expression for α given in Equation (2.25). The function $[(1+Z/2)/(1+Z)]$ F is plotted in Figure (2.2) as a function of the injection level factor Z and the material constant (τ_o/τ_∞). These curves are similar to those that have been published by Messenger.[5] They are believed to be more accurate in that a more exact expression has been used in the integration of the injected charge density over the base volume. This may be seen by comparing Equation (2.32) above with a similar expression in Messenger's paper.[5]

The effect of radiation on the current gain, as given now by Equation (2.40), follows directly from the expression for diffusion length degradation,

$$1/L^2 = 1/L_o^2 + K\varphi \quad , \tag{2.41}$$

where L_o is the unirradiated value, K is the damage constant, and φ is the time integrated high energy flux. With Equation (2.41), Equation (2.40) becomes,

$$\alpha(\varphi) = \alpha_o - KW^2 \quad (1 + Z/2)/(1 + Z) \quad F\left(Z, (\tau_o/\tau_\infty)\right)\varphi \tag{2.42}$$

where α_o is defined by Equation (2.40) with L_o substituted for L.

Equation (2.42) predicts a linear decrease of α with integrated flux. It may also be written in differential form,

$$(d\alpha/d\varphi) = -KW^2 \quad (1 + Z/2) \quad (1 + Z) \quad F\left(Z, (\tau_o/\tau_\infty)\right) \tag{2.43}$$

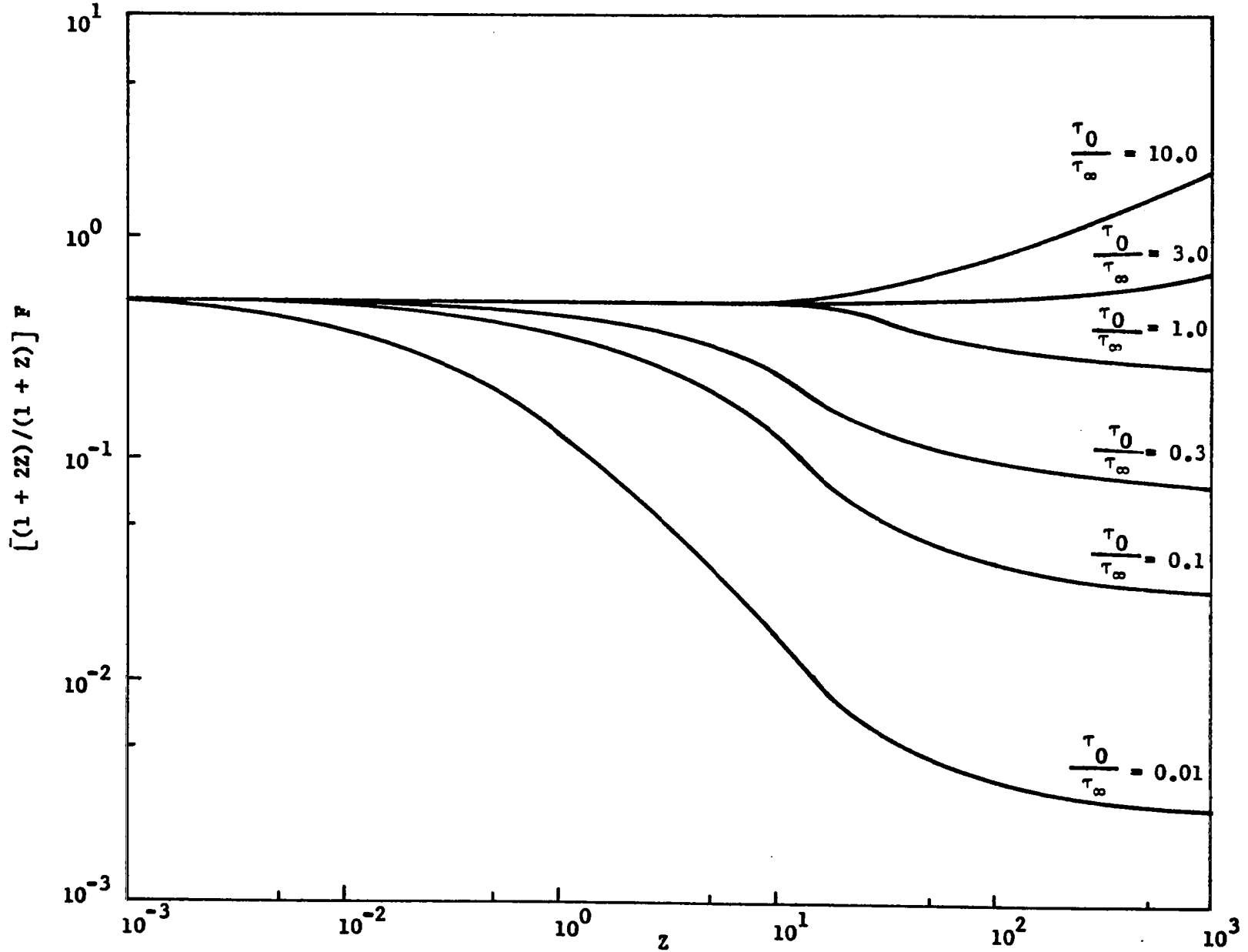
10^1
10^0
10^{-1}
10^{-2}
10^{-3}
$[(1 + 2Z)/(1 + Z)]$ F
10^{-3}
10^{-2}
10^0
10^1
10^2
10^3
Z
$\frac{\tau_0}{\tau_\infty}$ = 10.0
$\frac{\tau_0}{\tau_\infty}$ = 3.0
$\frac{\tau_0}{\tau_\infty}$ = 1.0
$\frac{\tau_0}{\tau_\infty}$ = 0.3
$\frac{\tau_0}{\tau_\infty}$ = 0.1
$\frac{\tau_0}{\tau_\infty}$ = 0.01

Under conditions of low level injection Equation (2.43) becomes,

$$(d\alpha/d\varphi) = -(W^2/2)K \qquad (2.44)$$

The important fact now apparent is that under conditions of high level injection the rate of degradation $(d\alpha/d\varphi)$ in Equation (2.43) is no longer dependent only on base width and damage constant, but is now dependent on the additional terms contained in the Z-factor, which are just those terms that were included in the design variations. It will be clear subsequently, in the Sections that follow on the experimental results, that injection level effects are important and that the more generalized expression for the current gain, α, given in Equation (2.42) is required for interpretation of the data and in providing a basis for more detailed design variation studies.

3.0 EXPERIMENTAL PROGRAM

3.1 Transistor Fabrications

The basic philosophy of a design effects program is to investigate the relationships between the fabrication procedures used in producing an existing semiconductor device and the rate of degradation of its electrical property in the high energy environment. In the present investigation a typical silicon planar transistor, known for its desirable radiation resistant properties, was chosen because the processes which determine its physical design parameters are well understood and easily controlled. Specifically, the 2N708 transistor is representative of a class of high frequency, multipurpose transistors which find many applications in electronic circuitry. During the initial planning phase of this program, each of the steps in the processing of a silicon planar transistor was examined to determine if a variable in that step might significantly modify the rate of degradation of the current gain.

To do this a table similar to Table(3-1)was constructed. In this table only those processes with the prospect of leading to alterations significant for radiation resistant design were considered. Processes such as slicing, dicing and chemical cleaning were excluded since they do not contribute to the geometrical or chemical impurity content of the finished device. The significant processing steps are listed in the first column and are related to the respective geometrical factors, impurity doping concentrations, or surface conditions which may be affected by the particular process. In each case, where a processing step was varied to produce a design variation, the lot numbers of those variations which were fabricated appear in the square together with the name of the variation. The term "N/A" is used to denote processing variations which were considered to

TABLE 3-1

PHYSICAL DESIGN PARAMETERS

PROCESSING STEP	GEOMETRICAL FACTORS	IMPURITY DOPING CONCENTRATIONS	SURFACE CONDITIONS
1. Crystal Selection		Czochralski vs Float zone material (Oxygen concentration) RR22	
2. Lap and Polish	N/A(1)		
3. Oxidized Epitaxial Growth		Epitaxial vs Nonepitaxial RR4A2, RR4B3, RR4C5	
4. Base Photo Resist	N/A(2)		
5. Base Diffusion and Oxidation	Steps 5 and 7 control the base width RR11, RR13, RR15	Base Doping Profile RR17, RR18	This oxide is etched off prior to Step 6.
6. Emitter Photo Resist	Emitter Geometry RR9A, RR10B, RR10C		
7. Emitter Diffusion and Oxidation	Base width RR11, RR13, RR15	Emitter and Base Doping Profile RR17, RR18	Surface conditions, Effect of HCl etch (3) RR7A, RR7B, RR7C, RR7D, RR1A, RR1D4, RR1G7
8. Gold Evaporation and Diffusion		Gold concentration RR1E5A, B; RR1F6A, B; RR1H8A, B	
9. Contacts, Headers, Bonding, and Encapsulation			

(1) Although this variation is not expected to influence the radiation resistance of the device, a thinner slide would compensate for the higher values of V_{SAT} encountered in the prototype variations.

(2) This process controls the collector base junction area which does not appear in the present design equations for displacement effects.

(3) The HCl etch refers to the process of removing the SiO_2 formed by the emitter and base diffusions.

have little or no effect on the device performance in a high energy charged particle environment.

An expanded form of Table (3-1) appears in Table (3-2). In Table (3-2) the design variations which were fabricated as part of this program are listed by lot number and the measured physical design parameters are given.

Ideally, when a particular design variation is under investigation, all of the other parameters should be held constant. Such a condition is not always possible to obtain. This is true for example in the emitter radius design variation. In this production run the test variations RR10A, RR10B, RR10C were produced during a simultaneous diffusion run, but the RR10A devices did not qualify to the 2N708 specifications; consequently, a "back-up" run was utilized to produce the 8 x 23 mil emitter geometry which was identified as lot number RR9A. A comparison of the design parameters of this device with lots RR10B and RR10C indicates an increase in the emitter carrier concentration resulting in an increased base width. Although the devices were not identical, the individual design variations are considered to be small in comparison with the effects which may be attributed to the variation in emitter geometry.

Each of the design variations shown in Table 3-2 were fabricated with the design goals shown in the first four columns in mind. After the devices were completed, the physical design parameters which characterize the device were taken and recorded in the last eight columns. In addition, a complete set of electrical characteristics, including BV_{CBO}, BV_{CEO}, I_{CBO}, I_{EBO}, $V_{CE(SAT)}$, h_{FE}, f_T, C_{ob}, and t_s, were measured on each of the 15 units produced for each design variation. In addition to the 2N708's with the design variations indicated, a particular design variation is also listed for a prototype radiation resistant

Table 3-2

Supplementary Physical Design Parameters

Design Variation	Variation	Lot No.	Base Width ($\times 10^{+4}$ cm)	Emitter Diameter ($\times 10^{+3}$ cm)	Gold Concentration (atoms/cm^3)	Emitter Doping ($\times 10^{-20}$ atoms/cm^3)	Base Sheet Resistivity (Ω/sq)	Base Junction Depth ($\times 10^{-4}$ cm)	Average Base Conductivity $(\Omega\text{-cm})^{-1}$	Base Surface Concentration ($\times 10^{-18}$ atoms/cm^3)	Emitter Sheet Resistivity (Ω/sq)	Emitter Junction Depth ($\times 10^{+4}$ cm)	Average Emitter Conductivity $(\Omega\text{-cm})^{-1}$	Average Emitter Concentration ($\times 10^{-20}$ atoms/cm^3)
Gold Concentration	No Gold	RR1E5A	1.5	3	0	5	85.5	4.2	28	7	2.57	2.7	1430	5
	1050°C Gold	RR1E5B	1.5	3	1.5×10^{16}	5	85.5	4.2	28	7	2.57	2.7	1430	5
	No Gold	RR1F6A	1.5	3	0	5	85.5	4.2	28	7	2.57	2.7	1430	5
	950°C Gold	RR1F6B	1.5	3	5×10^{15}	5	85.5	4.2	28	7	2.57	2.7	1430	5
	1050°C Gold	RR1H8A	1.5	3	1.5×10^{15}	5	85.5	4.2	28	7	2.57	2.7	1430	5
	950°C Gold	RR1H8B	1.5	3	5×10^{15}	5	85.5	4.2	28	7	2.57	2.7	1430	5
Emitter Radius	8 x 23 mils	RR9A	1.7	8 x 23	1×10^{16}	4	144.0	3.9	16					
	8 mils dia	RR10B	1.5	8	1×10^{16}	3	148.5	4.2	16	3	3.60	2.2	1250	4
	3 mils dia	RR10C	1.5	3	1×10^{16}	3	148.5	4.2	16	3	3.47	2.7	1060	3
										3	3.47	2.7	1060	3
Base Width	2.4 μ	RR11	2.4	3	1×10^{16}	3.5	144.0	5.1	14					
	1.5 μ	RR13	1.5	3	1×10^{16}	3.5	126.0	4.2	18	2.5	3.20	2.7	1160	3.5
	0.8 μ	RR15	0.85	3	1×10^{16}	3	117.0	1.95	43	4	3.15	2.7	1110	3.5
										11	9.45	1.1	960	3
Emitter Doping	High Doping	RR17	1.2	3	1×10^{16}	3.5	110.25	2.1	43					
	Low Doping	RR18	0.75	3	1×10^{16}	2	139.25	1.95	37	11	9.45	0.9	1180	3.5
										10	9.90	1.2	840	2
Surface Condition	No Pyrolytic	RR7A	1.1	3	1×10^{16}	3	105	4.5	19					
	Pyrolytic after base diff.	RR7B	1.1	3	1×10^{16}	3	105	4.5	19	4	3.15	3.4	935	3
										4	3.15	3.4	935	3
										4	3.15	3.4	935	3
	Pyrolytic on base after diff.	RR7C	1.1	3	1×10^{16}	3	105	4.5	19	4	3.15	3.4	935	3
	Pyrolytic glass	RR7D	1.1	3	1×10^{16}	3	105	4.5	19					
										7	2.57	2.7	1400	5
										7	2.57	2.7	1400	5
Etch and SiO_2	No Etch	RR1A												
	HCl Etch and SiO_2	RR1B4	1.5	3	1×10^{16}	5	85.5	4.2	28	6	2.25	3.3	1340	5
	HCl no SiO_2	RR1G7	1.5	3	1×10^{16}	5	85.5	4.2	28	-	-	-	-	-
Epi and Etch	Standard	RR4A2	1.8	3	1×10^{16}	4	81.0	5.1	24	-	-	-	-	-
	No Epi													
	Epi HCl	RR4B3	-	3	1×10^{16}	-	-	-	-	-	-	-	-	-
	Epi no HCl	RR4C5	-	3	1×10^{16}	-	-	-	-	4	3.15	2.1	1510	11
Czochralski vs Float Zone		RR22	1.5	3	1×10^{16}	11	140	3.6	19.9	10	7.2	1.6	820	2.5
Prototype		RR26	0.5	2.4	1×10^{16}	0.5	118	2.1	41					

device. This variation resulted from the results of the experiment outlined in Section 3.4.

In addition to the 2N708 investigation, and in accordance with the Work Statement, several multichannel field effect transistors were fabricated for radiation tests. These devices are unipolar transistors composed of a high density grid mesh of silicon p^+ material with cylindrical n type conducting channels. In each case the basic structure is a 10 x 10 Mil silicon chip with variations in channel number due to channel separation and diameter. These devices have ohmic contacts for source and drain and are intended for high frequency high power applications. Geometry 1 contains 380 channels with a channel diameter of 8.5 microns. Geometries 9 and 11 are 100 and 119 channel devices with 5 and 4.35 micron channel diameters respectively.

3.2 Instrumentation

The task of measuring the radiation induced degradation of the current gain of a large number of design variations requires a substantial degree of automation in the experimental instrumentation. The problem is compounded by the need to measure device parameters at several discrete operating points. For these reasons, the Hughes Automatic Data Acquisition System was utilized in measuring and recording the electrical parameters of interest in a systematic format which was compatible with the digital data reduction facilities at Hughes.

In the following discussion the critical components of this system are described in successively greater detail. Although the system is substantially more complex than shown in any of the following figures, this discussion is limited to those aspects of the system which directly affect the accuracy of the data and the reliability of the experimental results.

A block diagram and photograph of the Automatic Data Acquisition System (ADAS) are shown, respectively, in Figures (3-1) and (3-2). The system is divided into two subsystems; (a) a commutator and (b) a data accumulation system. The function of the commutator is to cycle through each device and each biasing condition and present the appropriate readout voltage of the data accumulation system. In addition, it provides the recording units with the proper identification signals to identify the number of the transistor and biasing circuit which is under test. The function of the data accumulation system is to control the sequencing of the commutator, measure the required circuit voltage, and record this signal together with its proper circuit and device identification on either a paper type punch or a parallel printer. After the initial checkout procedure for reproducibility the paper tape punch was used exclusively for recording the data.

A more detailed block diagram of the commutator system is shown in Figure (3-3). The number of bias conditions to be used to measure the dependence of current gain on level of injected carriers(emitter current) was determined by multiplying the number of decades of practical operating currents by the number of circuits to be used per decade. Measurements were limited to the range of emitter currents between two microamperes and twenty milliamperes. The lower value is limited by the magnitude of radiation induced leakage currents and the higher value is limited by the maximum collector current and the maximum power dissipation of the device. The discrete values of emitter current were determined by selecting three values spaced logarithmically for each decade of emitter current.

The transistors undergoing irradiation were connected to the device selector (a relay operated stepping switch) by fifty feet of insulated connecting wire. The device and test selectors were controlled by a sequencing circuit which chooses a specific device

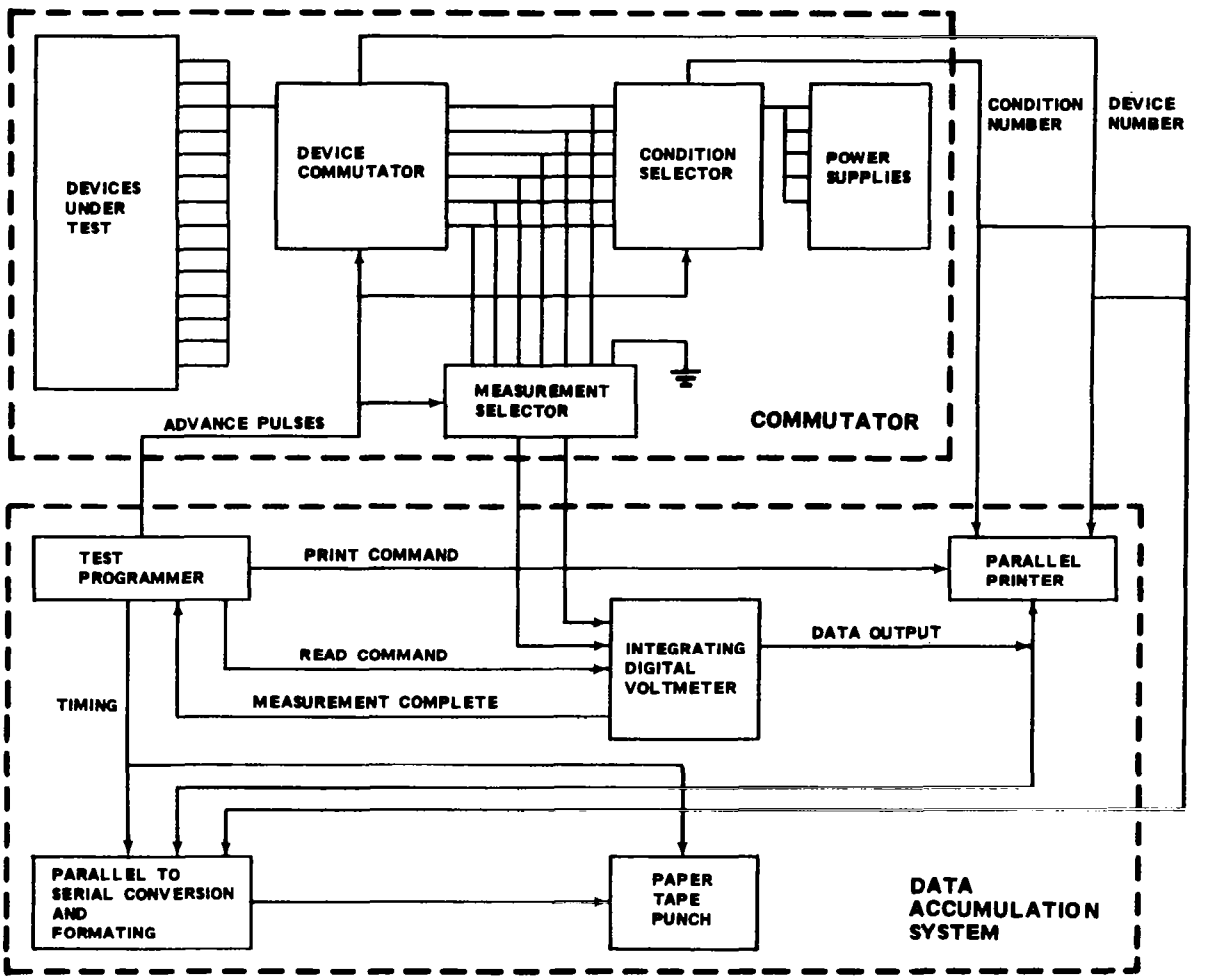

FIGURE 3-1 Automatic Data Acquisition System (Block Diagram)

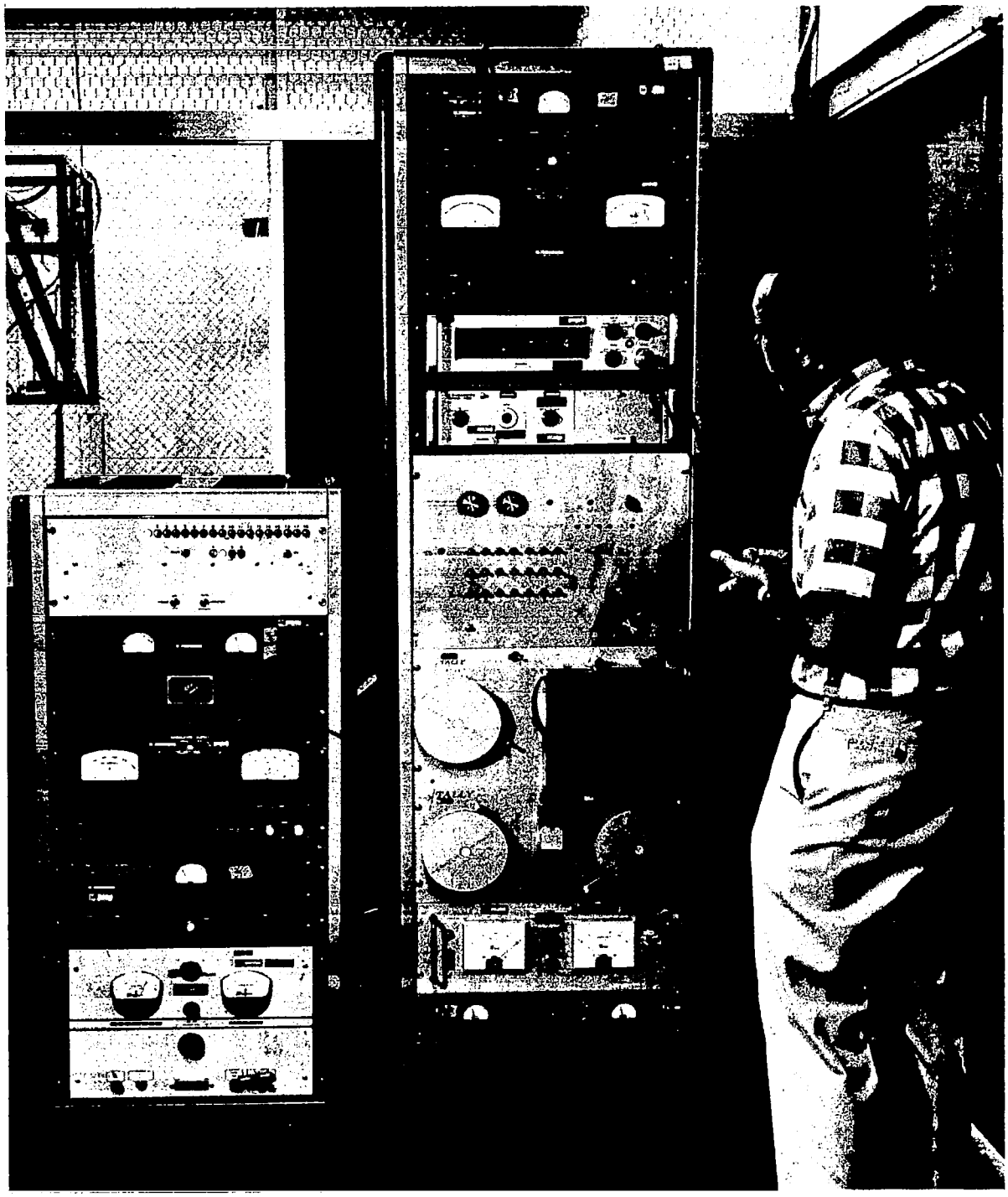

FIGURE 3-2 Automatic Data Acquisition System

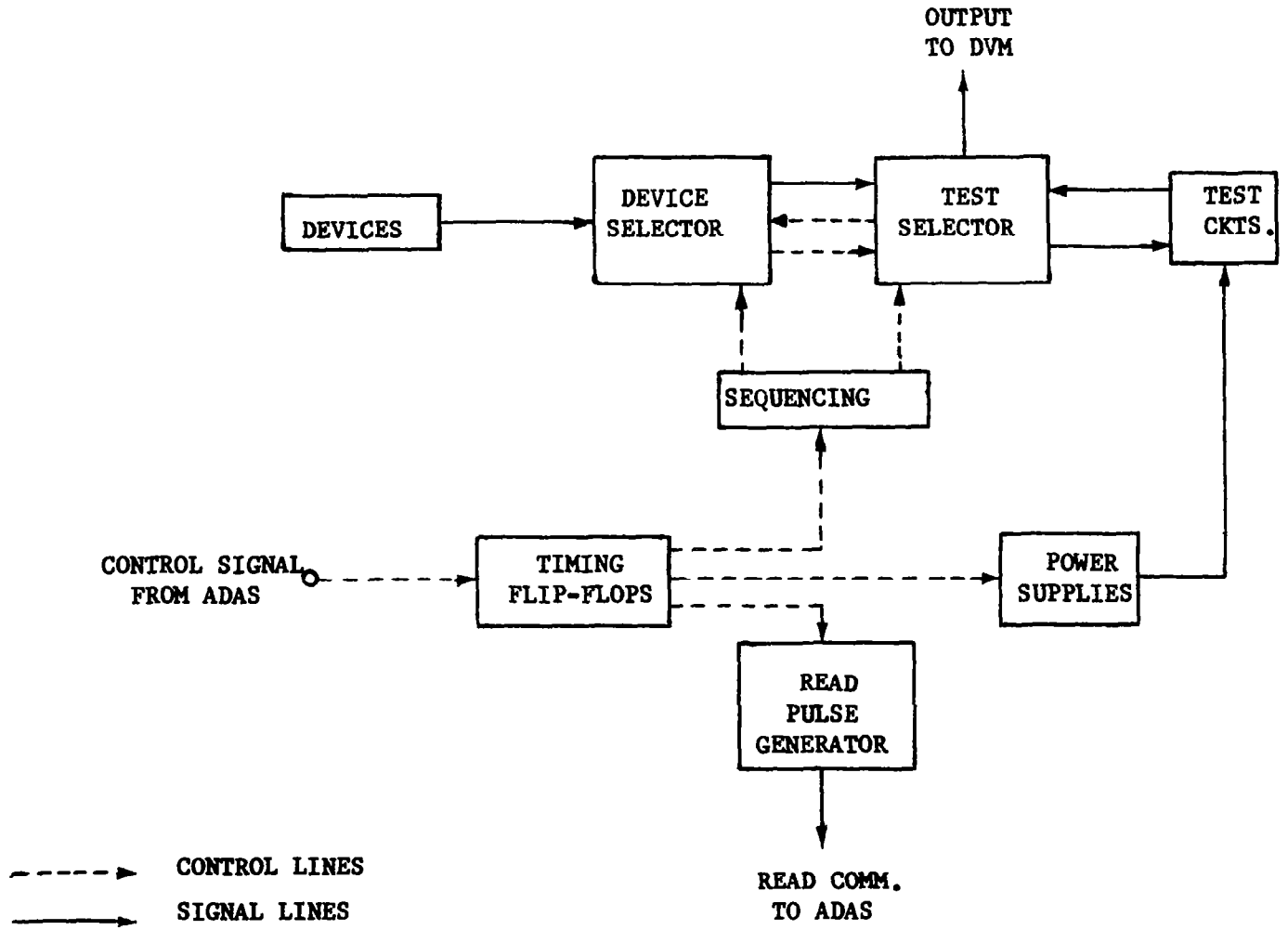

FIGURE 3-3 The Commutator System

and cycle through the various biasing conditions represented by each test circuit and returns to the next device in the sequence. The solid lines in Figure (3-3) indicate the signal path of the transistor responses and dotted lines show the path of the sequence control signals which originate with a flip-flop clock.

The test circuit appearing in Figure (3-4), with the circuit values given in Table (3-3), was used to measure the values of the common base current gain. By an appropriate slection of biasing resistors,

Table 3-3

Circuit Values for α Measurement

I_E	R_E (ohms)	R_C (ohms)	P_C (watts)
2 μa	50×10^6	0.5×10^6	2×10^{-6}
5 μa	20×10^6	0.2×10^6	5×10^{-6}
10 μa	10×10^6	0.1×10^6	1×10^{-5}
20 μa	5×10^6	50×10^3	2×10^{-5}
50 μa	2×10^6	20×10^3	5×10^{-5}
100 μa	1×10^6	10×10^3	1×10^{-4}
200 μa	0.5×10^6	5×10^3	2×10^{-4}
500 μa	0.2×10^6	2×10^3	5×10^{-4}
1 ma	0.1×10^6	1×10^3	1×10^{-3}
2 ma	50×10^3	500	2×10^{-3}
5 ma	20×10^3	200	5×10^{-3}
10 ma	10×10^3	100	1×10^{-2}
20 ma	5×10^3	50	2×10^{-2}

it is possible to obtain an accurate determination of the value of $\alpha(I_E)$ by measuring a single voltage. The resistor values shown in Table (3-3) were selected with the following criteria:

(1) The emitter circuit will form a constant current supply to control the level of injection, i.e., $R_E >> R_{BE}$.

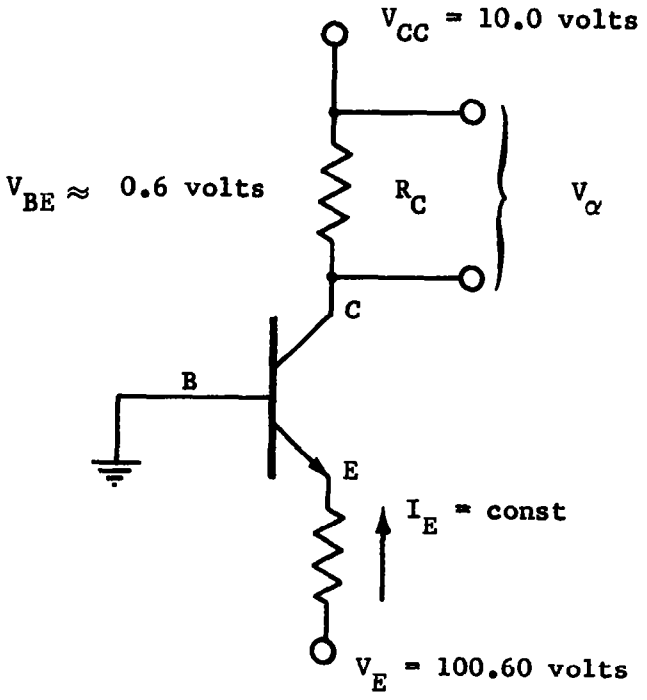

FIGURE 3-4 Circuit for α Measurement

(2) The emitter and collector resistors will complement one another to obtain a direct reading of α from the voltage (V_α) across the collector load resistor.

(3) The emitter voltage will compensate for the voltage drop across the emitter-base junction. (i.e., V_E = 100 volts + ΔV_{BE}, $\Delta V_{BE} \approx 0.6$ volts.)

(4) The actual collector voltage will remain relatively constant to avoid changes in gain due to operating point. (i.e., since $\partial I_C/\partial V_C$ is finite, the variation in $\partial V_C/\partial I_E$ must be held to a minimum.)

(5) The values of the resistors shown in Table(3-3)were selected to be less than the values shown in the Table by less than 0.01%. This allows the actual value of α to be determined to an accuracy of better than 0.1%.

(6) The value of the resistors was always sufficiently large to make voltage drops encountered in the connecting wires to be insignificant in comparison with the readout voltage.

Hence for a transistor with an infinite gain, the voltage V_α will be 1.000 volts. The value of the emitter voltage was reset before each data run on a regulated power supply to be V_E = 100.60 $\pm$ .01 volts.

The overall performance of the data acquisition system was excellent. Virtually all of the data taken maintained three significant figures. The ADAS specifications are listed in Table (3-4).

The paper tape used to record the data was arranged in a suitable

format to identify each bit of data and both the data and the identification signals were recorded in a binary coded decimal system. The Hughes 330B computer was utilized to read the paper tapes, convert to base ten voltages and record the data on a typewritten format suitable for plotting and data reduction.

Table 3-4

Automatic Data Acquisition System Specifications

Parameter	Value
DC Sensitivity	.01 - 1000 volts full scale
Maximum Frequency	10 KC
Repetition Rate	2 readings per second
Accuracy (voltmeter)	$\pm$ 0.01%
Accuracy (ADAS)	$\pm$ 0.1%

3.3 Experimental Procedure

Device irradiations were performed with 1 and 8 Mev electrons and with 31 Mev protons. The major part of the data was taken with 31 Mev protons at the University of Southern California proton LINAC facility. Figure (3-5) shows the transistor jig in front of the beam port at the USC proton LINAC. The proton irradiation data was supplemented with electron irradiations at 1 Mev with a GE Electron Beam Generator (EBG). The EBG facility is illustrated in Figure (3-6). Further electron irradiations at 8 Mev were performed at the Hughes Research LINAC Facility. The latter tests were carried out to check the dependence of the results on electron energy. A photo of the Hughes Research LINAC is presented in Figure (3-7).

Preliminary irradiations were conducted in February of 1965 with the EBG on units that were available from another program. This test furnished initial data on 2N708 degradation and served to

FIGURE 3-5 Experimental Layout at the USC Proton LINAC Facility

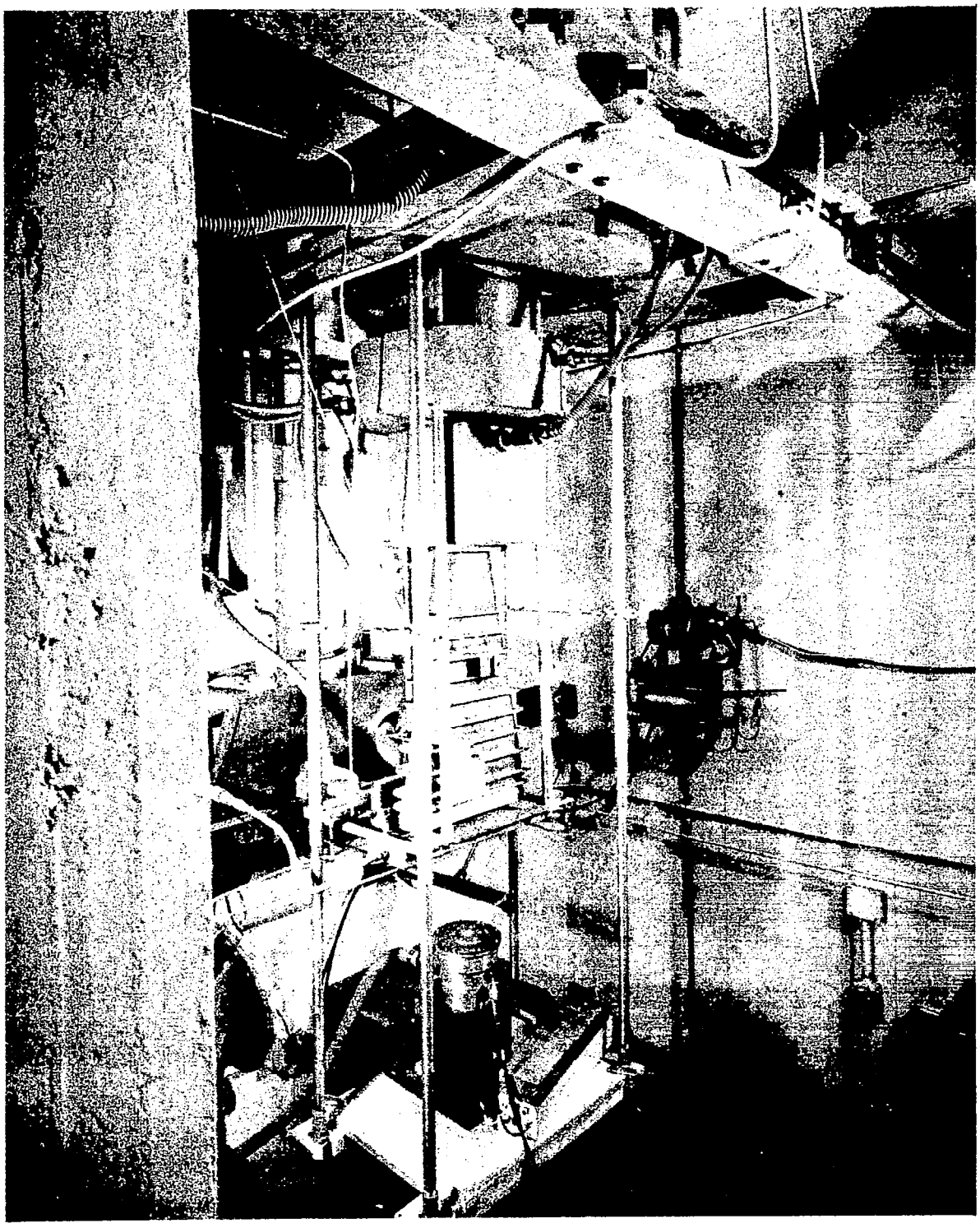

FIGURE 3-6 GE Electron Beam Generator with Faraday Cup

FIGURE 3-7 Hughes Research LINAC

delineate the integrated flux level at which degradation would occur. The main experimental effort was begun early in June at the USC proton LINAC. This was followed closely by irradiations at the Hughes Research LINAC and a return trip to USC later in the month. Final irradiations of the developmental devices were conducted at the EBG facility in September just before construction of the prototype radiation resistant device. Comparison of the prototype to standard 2N708's was made at the USC proton LINAC near the middle of October.

The proton LINAC beam current was measured by collecting the protons on a lead block and measuring the absolute current. Beam currents measured were the order of 2 nano-amps. Immediately after this reading was taken the sample mount was put in place with an ionization chamber behind it to provide relative current monitoring throughout the irradiation. The inhomogeneity of the beam cross section was monitored by exposing a glass slide before each socket exposure. The variation across the 3/4 inch collimator, as determined with densitometer readings of the glass slides, was approximately 30%. To insure that the results were independent of this inhomogeneity, several devices of each type were irradiated such that each device would appear in as many socket positions as time would permit. Analysis of variance techniques, to be described below, were used to remove the positional dependence of the device response.

The total electron current at the Hughes Research LINAC was monitored before each irradiation be collecting the electrons on a tungsten target that served as a beam catcher. Typical currents were the order of 250 ma. The beam spread and socket position was such as to give a current density constant to within 10% over a 3/4 inch diameter. The cross section of the beam was measured by utilizing the radiation induced current response of 2N708 transistors previously calibrated against a p-n junction nuclear

detector. From a knowledge of the beam cross section and total current, the current density in the central uniform area was determined.

The Electron Beam Generator provides a uniform irradiation over an area large compared to the size of the sample mount. The effective current density at the socket position was determined with a Faraday cup and 3/4 inch collimator. The variation across the 3/4 inch circle was determined with glass rods for ultraviolet fluorescence dosimetry.

In each radiation test the transistors were mounted four at a time in a twelve-pin tube socket and placed such that the beam entered through the top of the can. The transistors were unbiased during irradiation. At the end of each irradiation interval electrical measurements were made while the transistors were still in position with the Automatic Data Acquisition System described in Section 3.2. Exposure intervals were selected so that each socket was exposed to an integrated flux such that the common emitter current gain would drop 80% in approximately seven equal time intervals.

A different procedure was used for the multichannel field effect devices. At the end of each exposure interval drain current as a function of drain voltage characteristic curves were displayed on a curve tracer and photographed. The FETs were unbiased during irradiation. Because of the size of the FET cans relative to the collimator they were irradiated one at a time.

3.4 Experimental Results and Comparison with Theory

3.4.1 Results of Experiment

As discussed in Section 3.1 on device fabrication, transistors were constructed in which a single design feature was

varied while in other respects the design was standard. These units were then irradiated and examined to determine the effect of each design variation upon radiation resistance. From this data an optimum design was drawn for the construction of the prototype radiation resistant device. In the examples which follow, the initial design features are compared against each other and against the prototype. This is followed by a comparison between the prototype and standard 2N708's from three leading manufacturers.

Correlation of design variations to radiation resistance was found to be pronounced in five of the design variations investigated. These design features are (a) emitter geometry, (b) emitter doping, (c) base width, (d) collector gold concentration, and (e) Czochralski and float zone material. In each case the data taken at all radiation tests was consistent. As discussed previously the common base circuit leads to a direct determination of the DC current gain α, for a range of constant emitter currents. This parameter, therefore, serves as a convenient measure of the radiation degradation. In Figures (3-8), (3-9), and (3-10) the dependence of α on integrated proton flux is plotted for the emitter geometry variation. The data is taken for a range of constant emitter current, as shown, from 100 μa to 10 ma. The important fact that is evident in these results, as in the results for the other variations, is the linear or near linear variation of α with integrated flux and, in addition, the dependence of the slope on the emitter current or injection level with the slope decreasing with increasing level of injection. As a consequence of this linearity, the degradation of α can also be characterized by plotting the slope ($d\alpha/d\Phi$) as a function of emitter

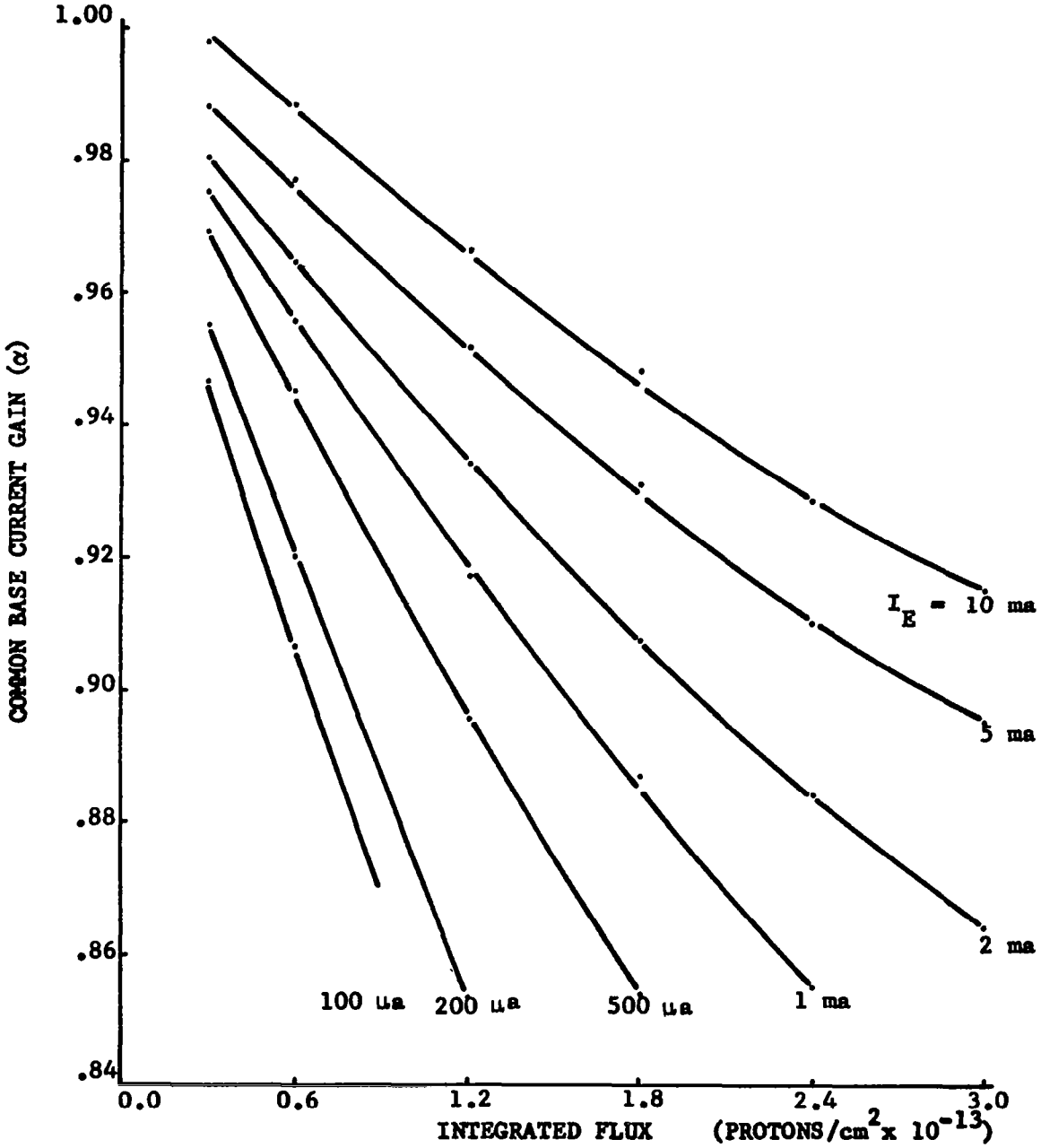

FIGURE 3-8 Degradation of α Under 31 Mev Proton Irradiation. Emitter Geometry Variation 8 x 23 Mils

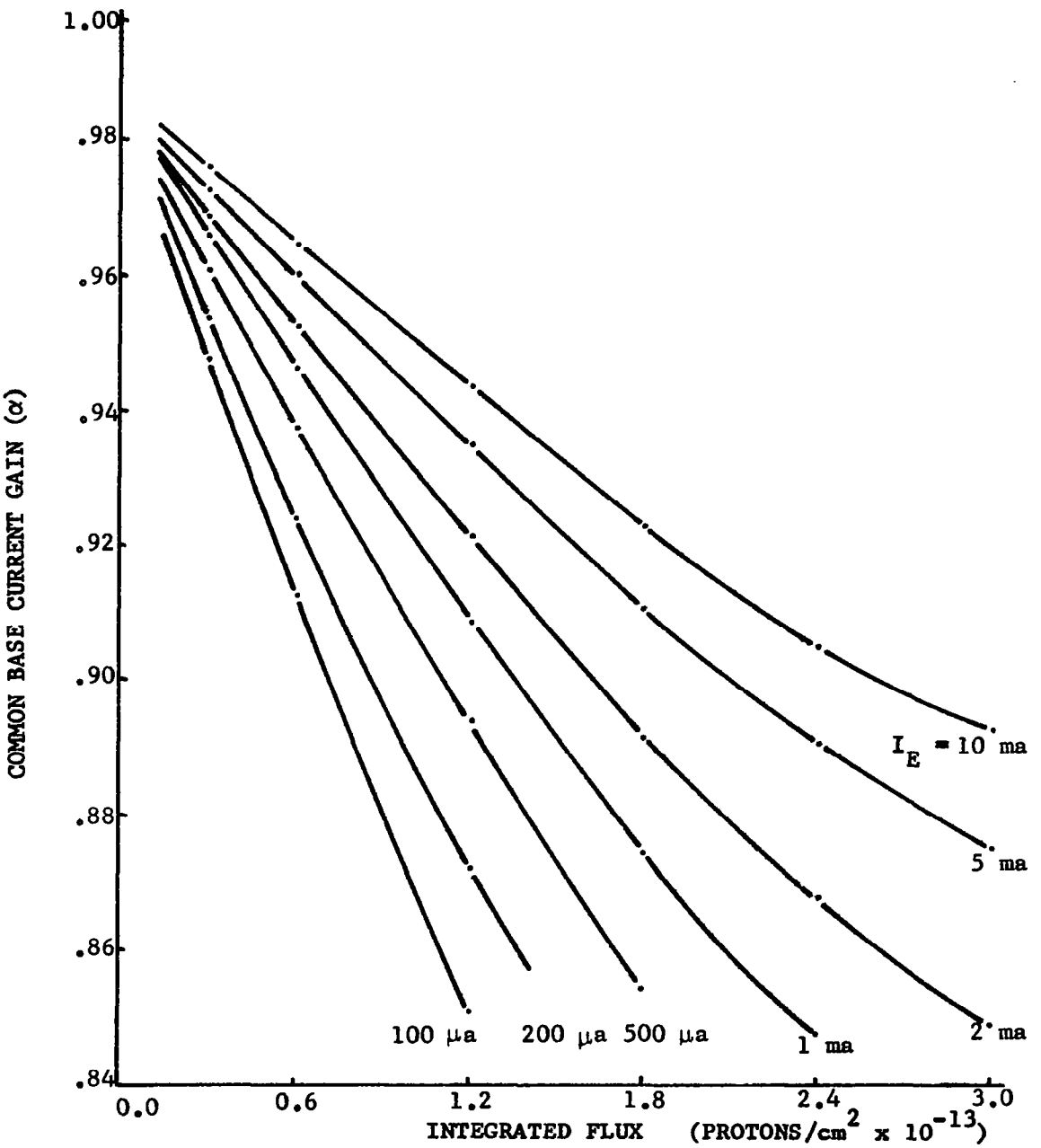

FIGURE 3-9 Degradation of α Under 31 Mev Proton Irradiation, 8 Mil Emitter Diameter

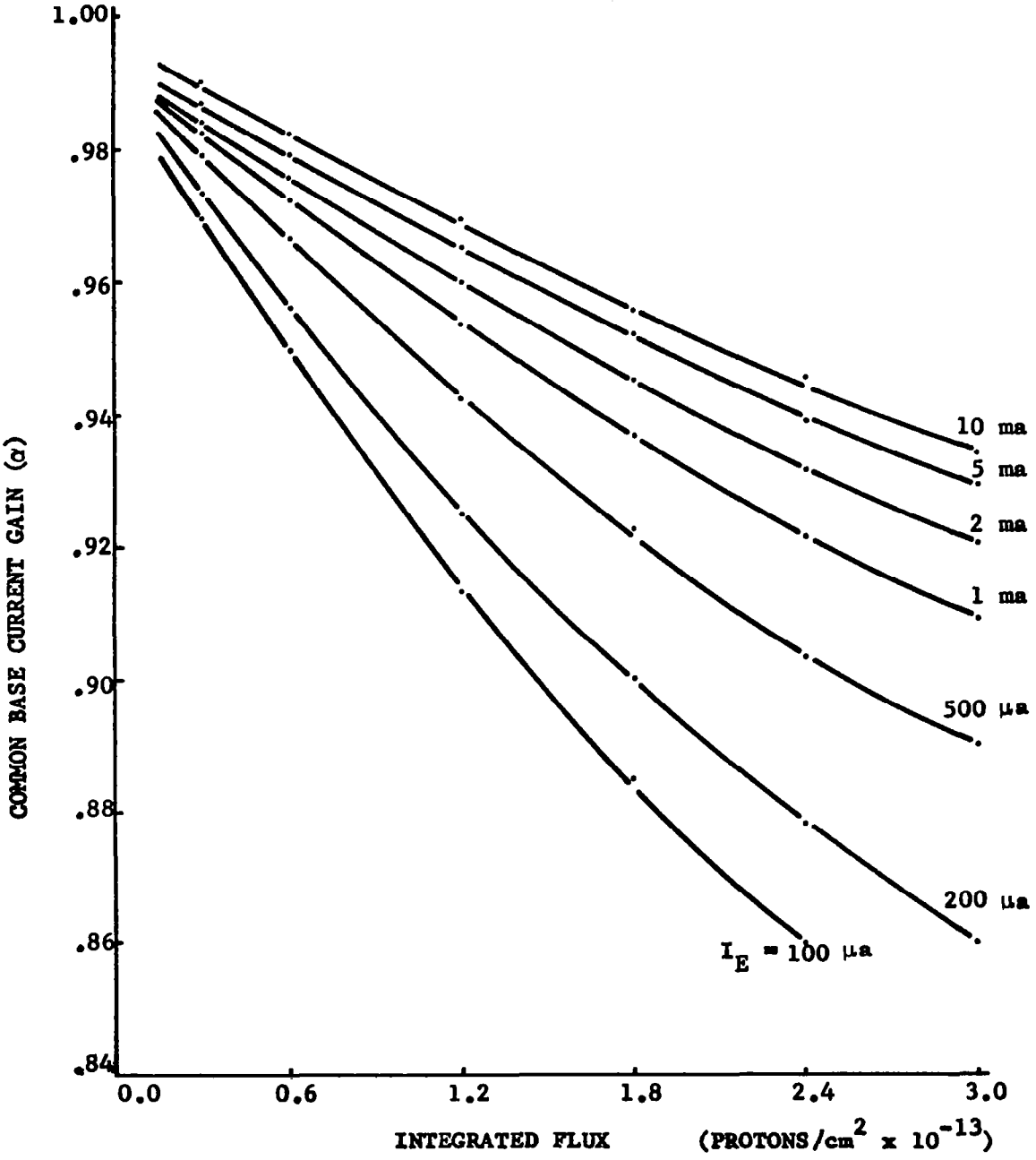

FIGURE 3-10 Degradation of α Under 31 Mev Proton Irradiation. 3 Mil Emitter Diameter

current at a given integrated flux. This method of plotting has the advantage of summarizing on a single graph the results for a single variation. The results for the emitter area variations are presented with this type of plot in Figure (3-11). In a plot of $d\alpha/d\varphi$ as a function of I_E (the absolute value of the slope is taken) a low value of the slope indicates a high radiation resistance. It will be noted that as the radiation resistance improves, the slope becomes less dependent upon the emitter current. The same comparative results among the different variations were obtained under electron irradiation. Two emitter areas for example are compared in Figure (3-12) for electron irradiation. These results may be compared with the similar ones for proton irradiation in Figure (3-11). The next four Figures, (3-13) through (3-16), are similar plots of $d\alpha/d\varphi$ for each of the other design variations. On each plot the response of the prototype is presented to illustrate the effect of combining in the prototype all the optimum design features. It should be noted that the prototype data was collected at a later date and some of the variation will be due to positional effects as mentioned in Section 3.3.

In the final radiation tests at USC, the prototype device (design specifications given in Section 3.1 was compared to standard 2N708's from three leading manufacturers. Typical results from this irradiation test are shown in Figure (3-17). The experiment was arranged such that each device appeared in each socket position. The arrangement is described in Table 3-5.

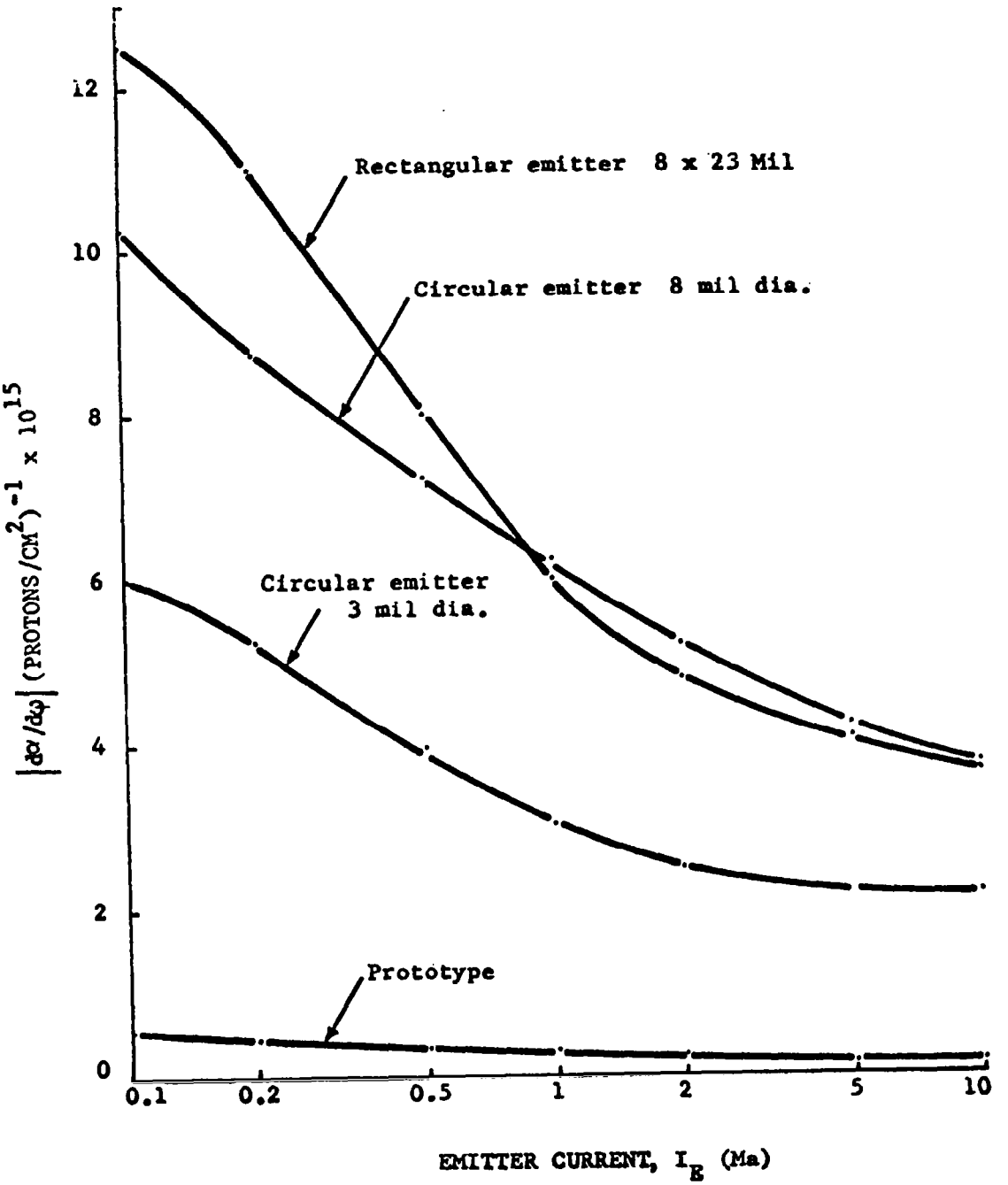

FIGURE 3-11 Rate of Degradation of α Under 31 Mev Proton Irradiation

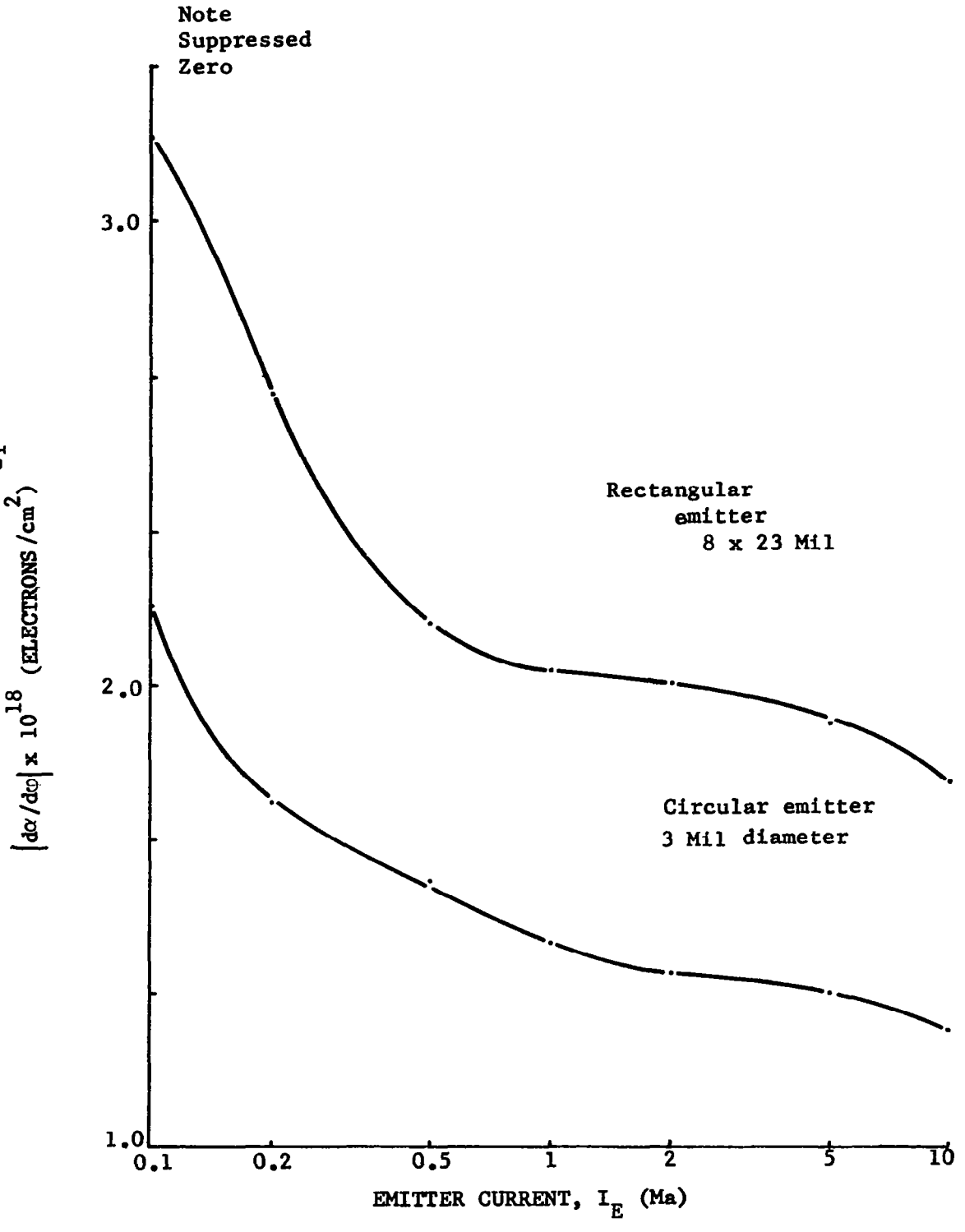

FIGURE 3-12 Rate of Degradation of α Under 1 Mev Electron Irradiation

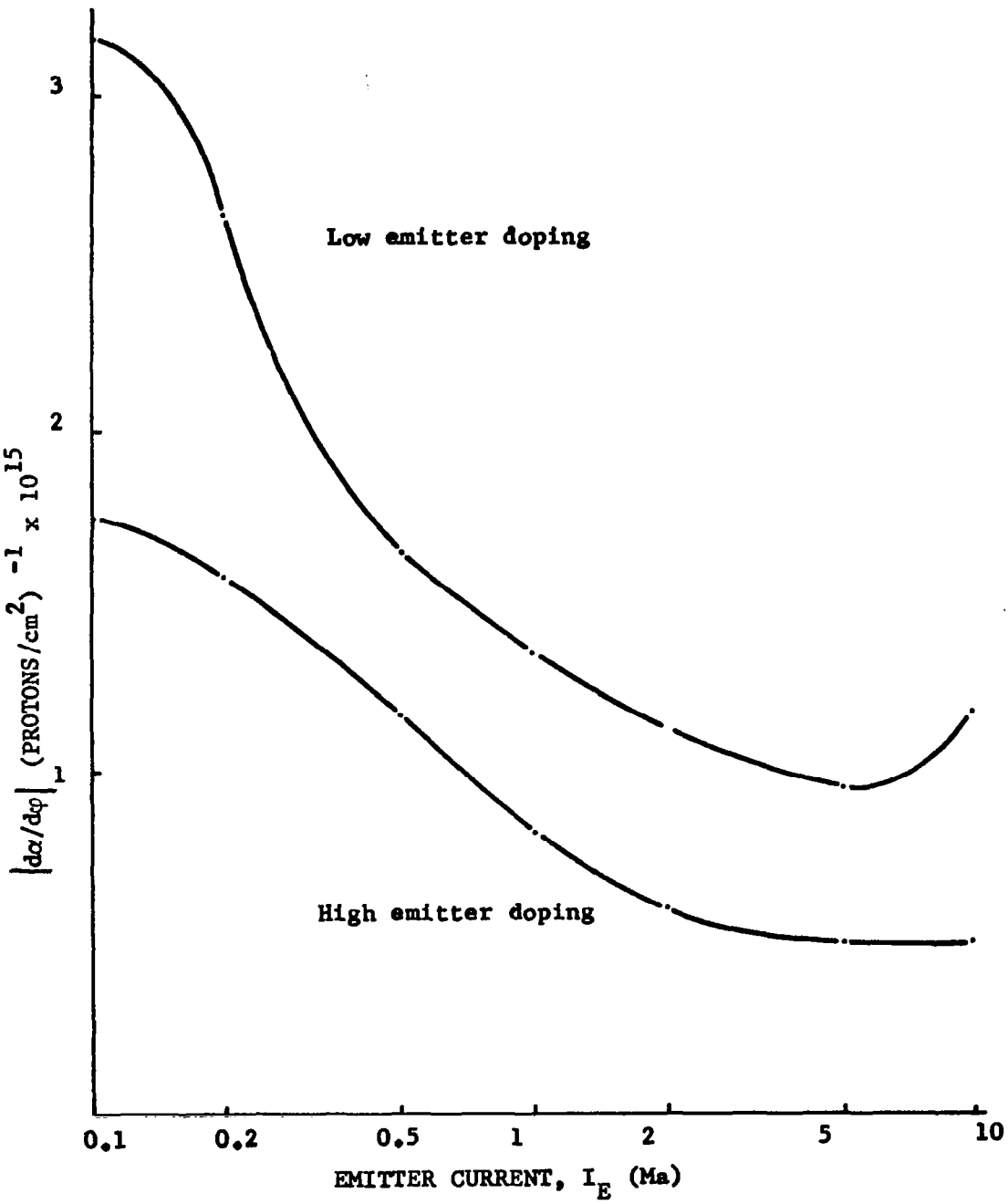

FIGURE 3-13 Rate of Degradation of α Under 31 Mev Proton Irradiation

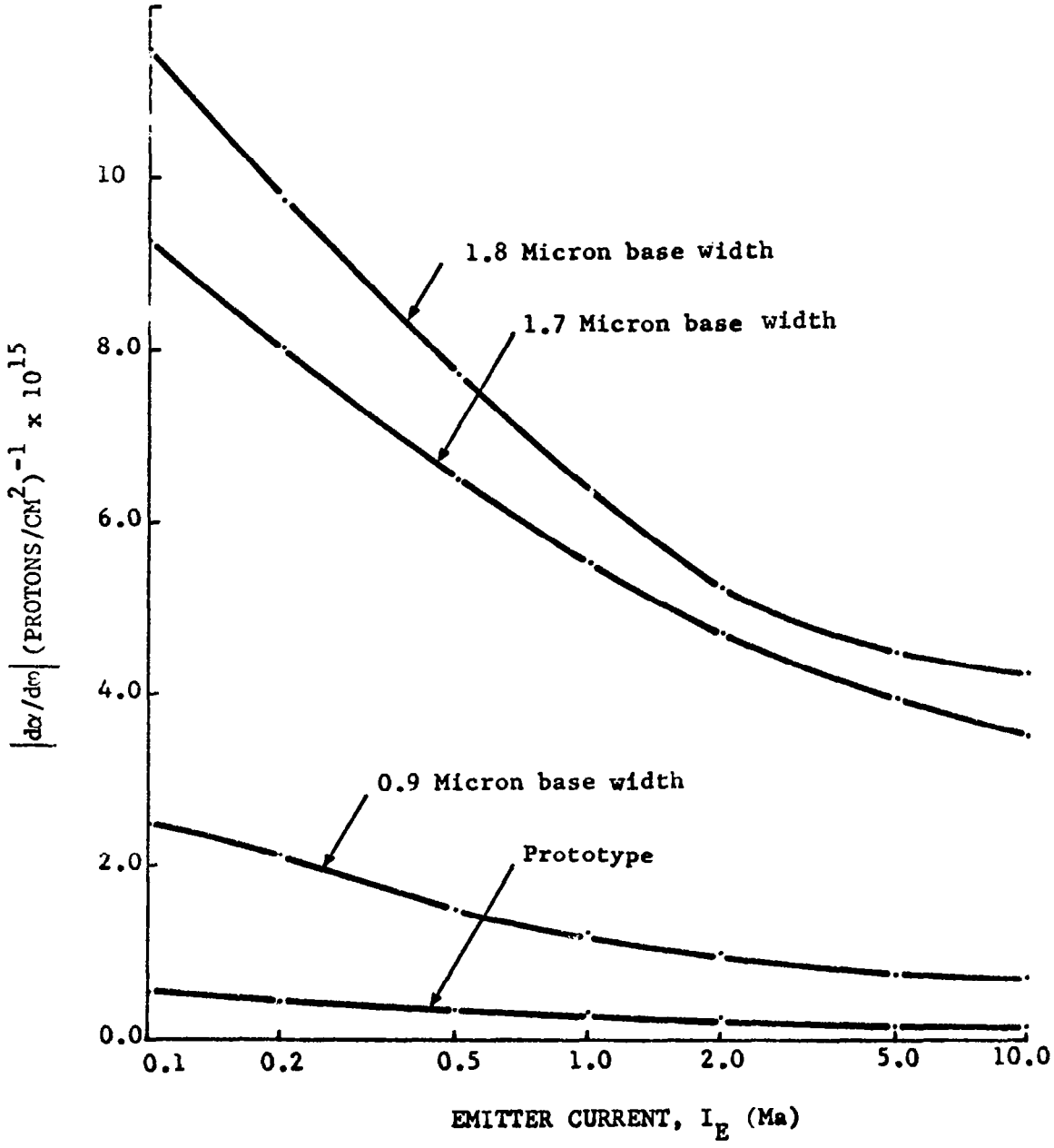

FIGURE 3-14 Rate of Degradation of α Under 31 Mev Proton Irradiation

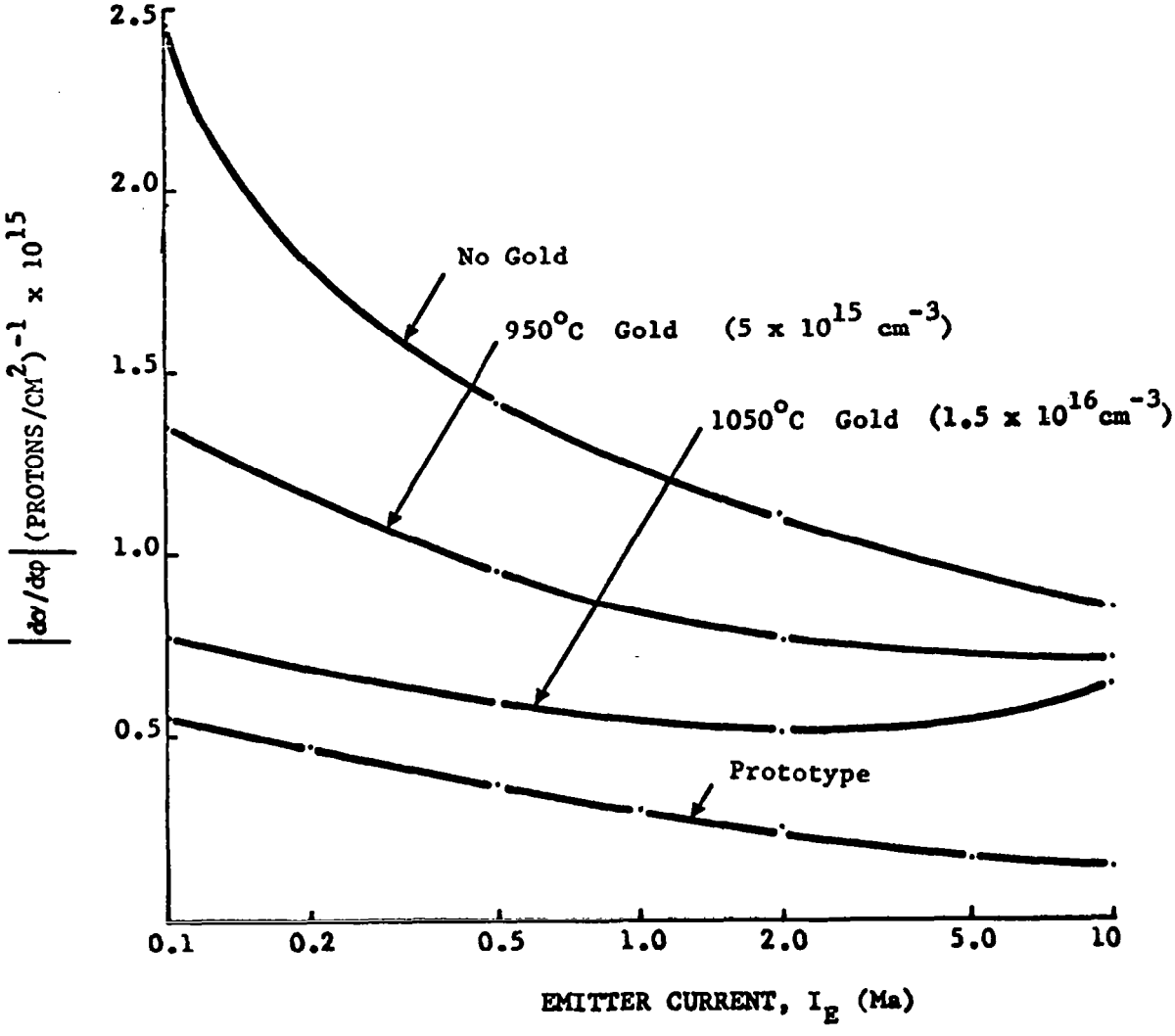

FIGURE 3-15 Rate of Degradation of α Under 31 Mev Proton Irradiation

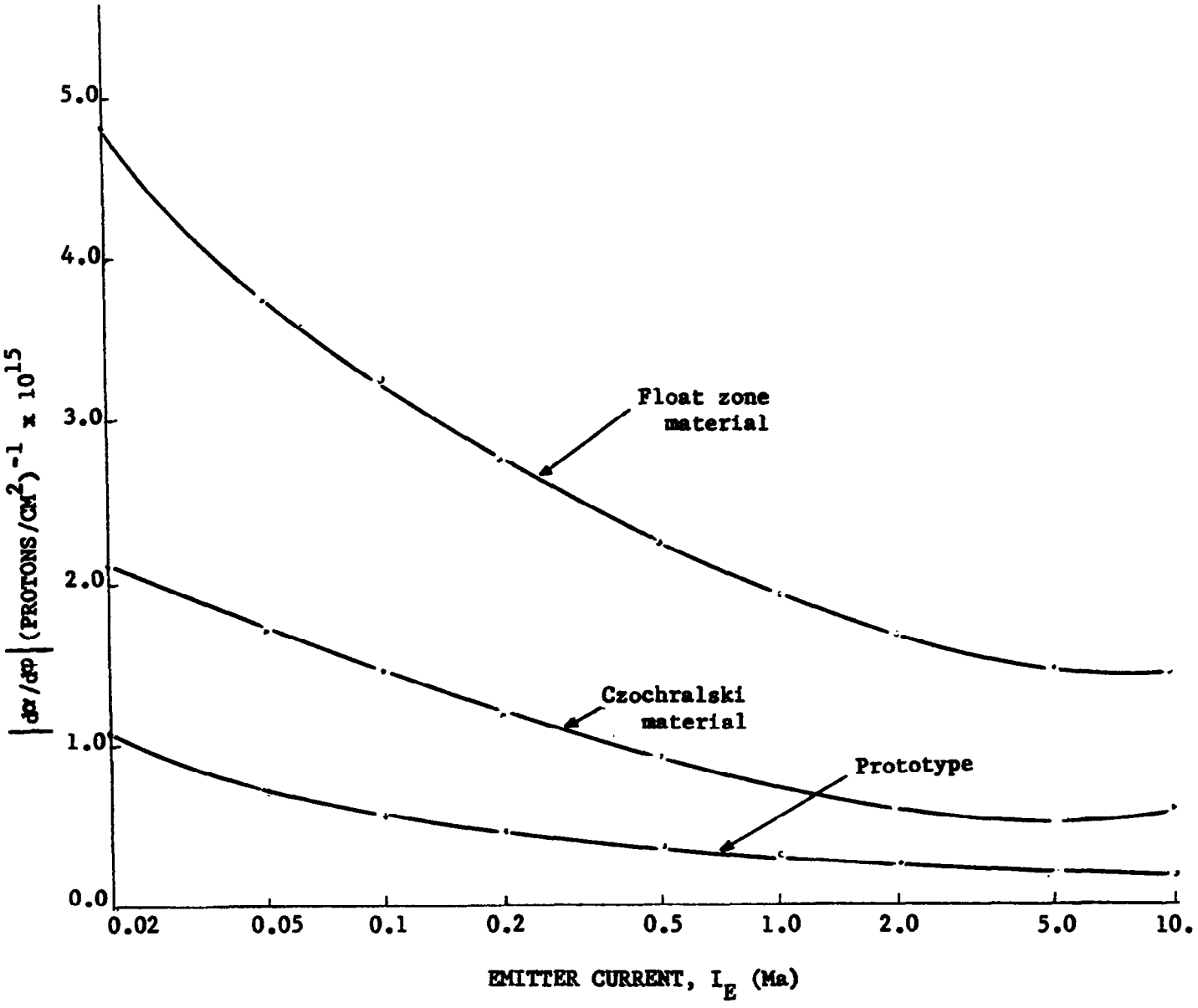

FIGURE 3-16 Rate of Degradation of α Under 31 Mev Proton Irradiation

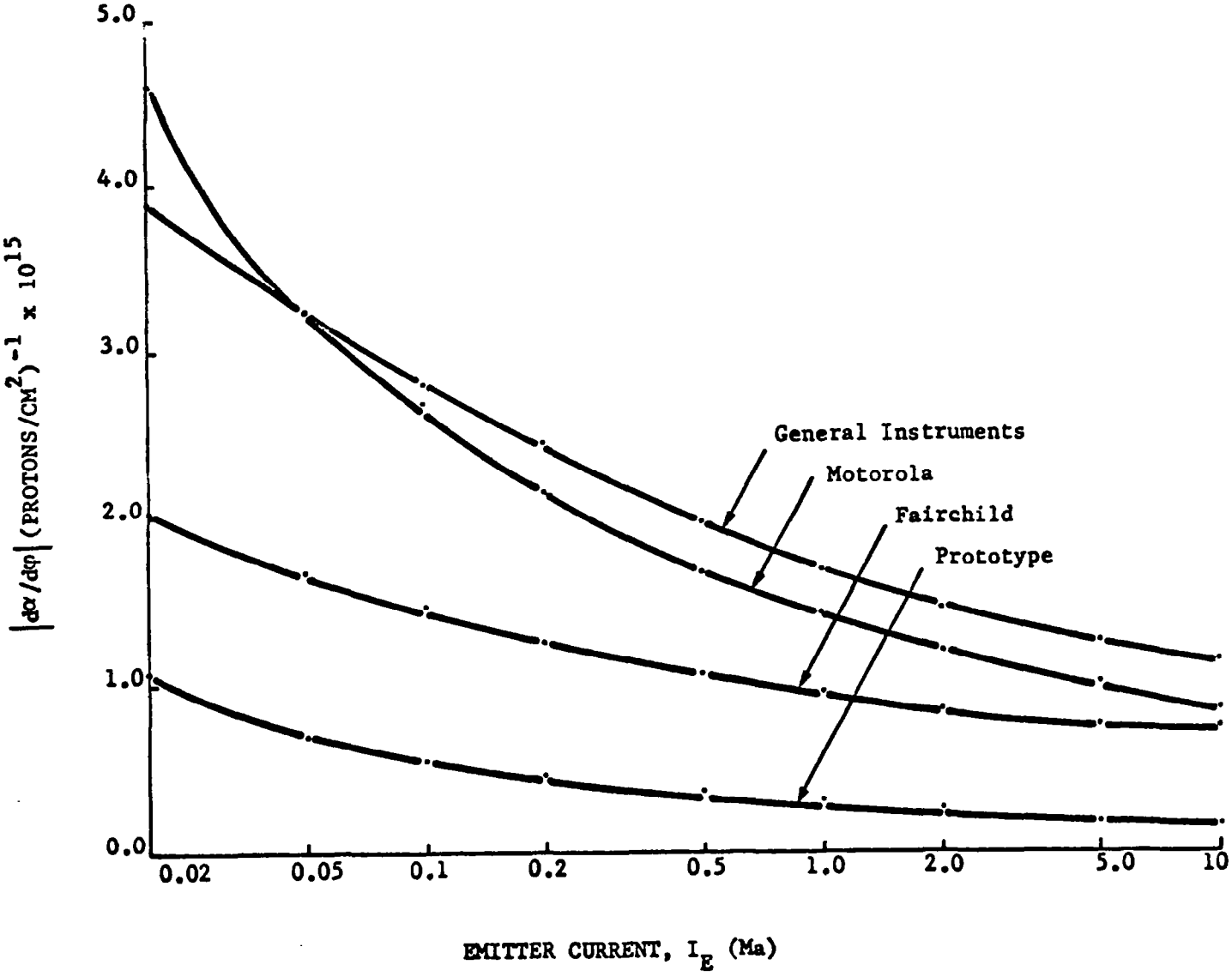

FIGURE 3-17 Rate of Degradation of α Under 31 Mev Proton Irradiation

Table 3-5

Device Arrangement for Statistical Analysis

Position/Socket	1	2	3	4	5
1	F	M	GI	H	HP
2	M	GI	H	HP	F
3	GI	H	HP	F	M
4	H	HP	F	M	GI

where F = Fairchild Standard
M = Motorola Standard
GI = General Instruments Standard
HP = Hughes Prototype
H = Hughes Standard (special production)

For comparison the rate of degradation in arbitrary units at an integrated flux of 1.5×10^{13} protons/cm^2 and an emitter current of 100 μamps was selected. The data for the Motorola device (M) in sockets 1 and 4, as well as that for the Hughes standard (H), was lost due to leakage effects. The experimental data, arranged by position and type, is presented in Table 3-6,

Table 3-6

Results of Prototype vs Standard Irradiation

Position/Type	F	M	GI	HP	
1	1.87	2.40*	2.40	1.35	$\bar{X}_r$ = 1.87
2	0.86	1.63	1.68	0.33	$\bar{X}_r$ = 1.13
3	0.82	1.26	0.98	0.83	$\bar{X}_r$ = 0.97
4	1.05	1.43*	1.25	0.40	$\bar{X}_r$ = 0.90
	$\bar{X}_c$=1.15	$\bar{X}_c$=1.45	$\bar{X}_c$=1.58	$\bar{X}_c$ = 0.73	

where asterisks indicate values for the missing data determined by standard analysis of variance techniques,[8] but not included in the calculation of mean values, and where X_c and X_r refer to column and row mean values respecitvely.

Using analysis of variance techniques, the following conclusions may be drawn from the data:

1. A significant difference between types and positions exists at a 0.5% confidence level when the hypothesis of equality is examined. That is, there is a 99.5% likelihood that a significant difference exists.
2. There is no significant difference in integrated flux between positions 2, 3, and 4, but the integrated flux at position 1 is greater, at the 0.5%, 0.1%, and 0.1% confidence level, respectively than for positions 2, 3, and 4.
3. The Hughes prototype degradation rate is lower than that of the Fairchild, Motorola, and General Instruments at the 2.5%, 0.5%, and 0.05% confidence level. That is, after positional variations are eliminated, there is a 97.5%, 99.5% and 99.95% probability that the Hughes prototype has a lower degradation rate than the Fairchild, Motorola, and General Instruments devices, respectively.

Following the procedure outlined in Section 3.3, three multichannel FET's were irradiated at the USC proton LINAC The results of these irradiations, as recorded on curve tracer photographs, are presented in Figures (3-18), (3-19), and (3-20). As discussed in Section 3.1 on transistor fabrication, the devices of geometries 9 and 1 were made on silicon chips, each 10 x 10 mils. The irradiation of

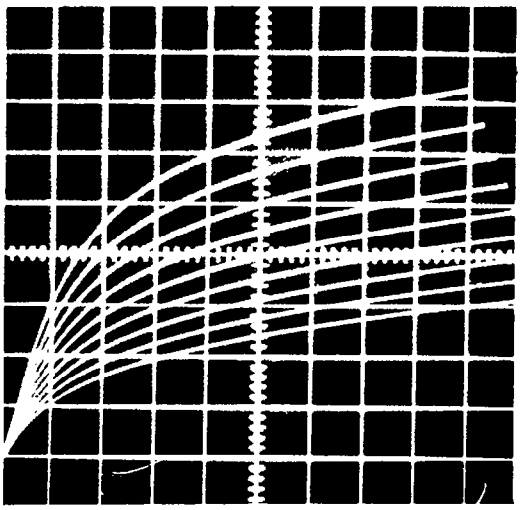

Pre Test
Vertical 5 ma/div
Horizontal 2v/div
Gate 0.5v/step

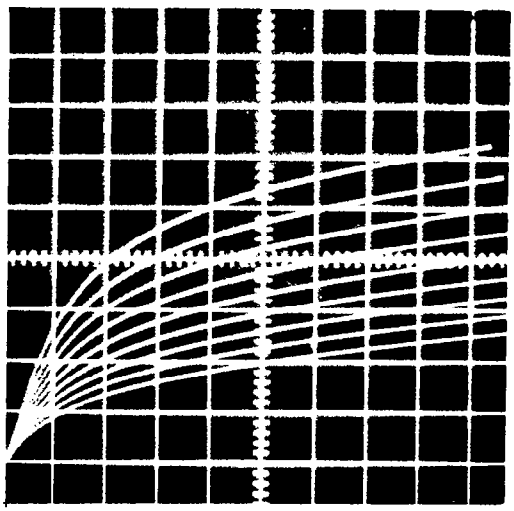

Integrated Flux 1.18×10^{13} protons/cm^2
Vertical 5 ma/div
Horizontal 2v/div
Gate 0.5v/step

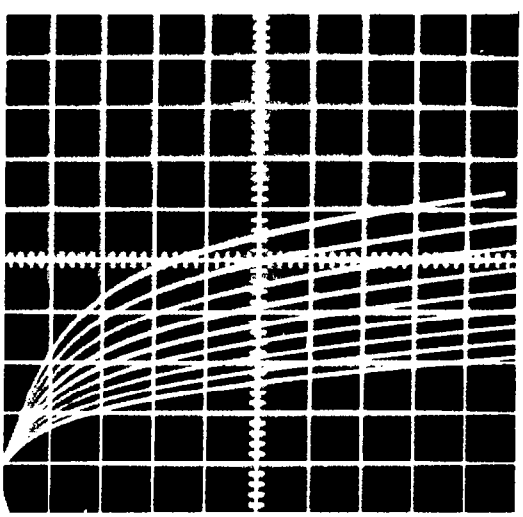

Integrated Flux 2.36×10^{13} protons/cm^2
Vertical 5 ma/div
Horizontal 2v/div
Gate 0.5v/step

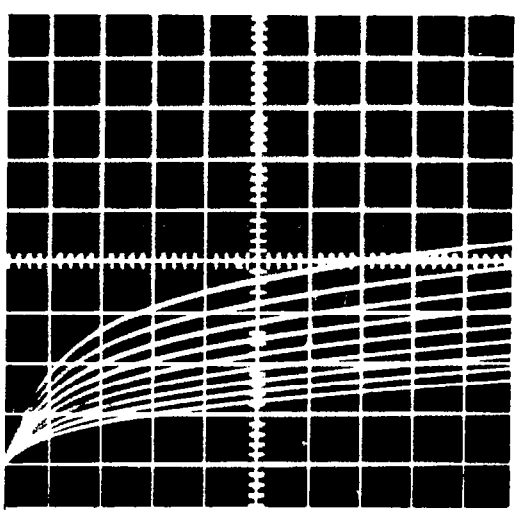

Integrated Flux 3.54×10^{13} protons/cm^2
Vertical 5ma/div
Horizontal 2v/div
Gate 0.5v/step

FIGURE 3-18 Drain Current Characteristics for Geometry No. 11, 169 Channel FET

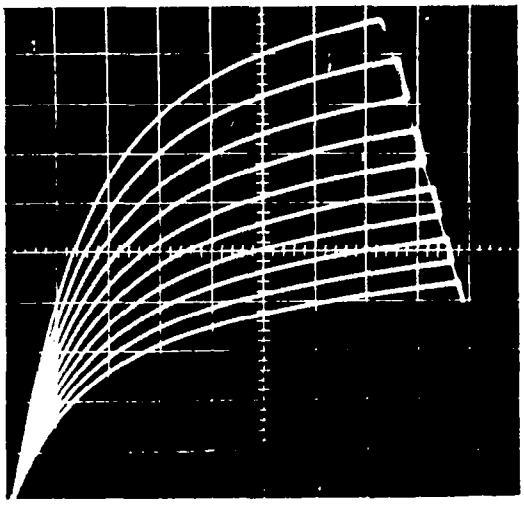

Pre Test
Vertical 2 ma/div
Horizontal 2v/div
Gate 0.5v/step

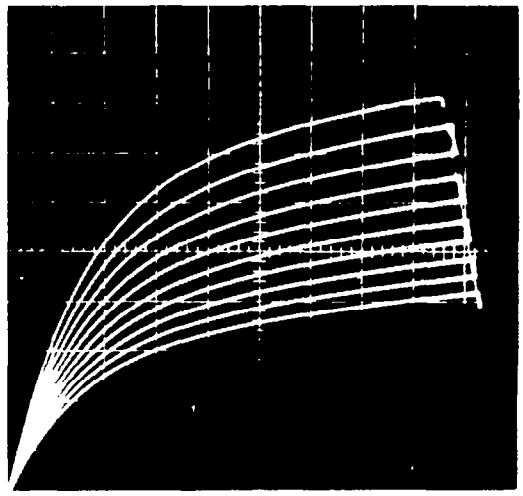

Integrated Flux 2.25 x 10^{13}
protons/cm
Vertical 2 ma/div
Horizontal 2v/div
Gate 0.5v/step

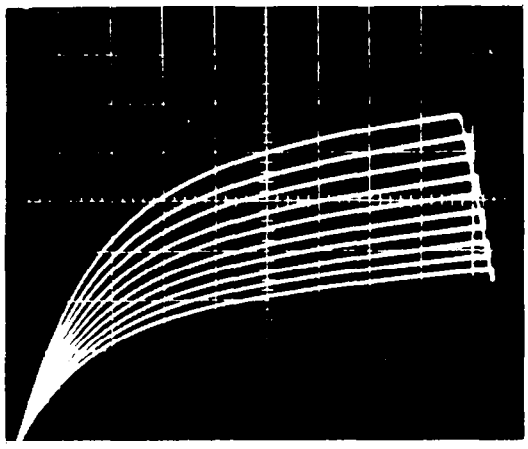

Integrated Flux 3.75 x 10^{13}
protons/cm^2
Vertical 2ma/div
Horizontal 2v/div
Gate 0.5v/step

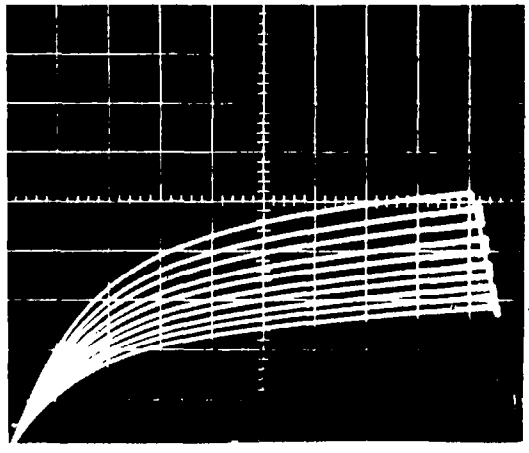

Integrated Flux 5.25 x 10^{13}
protons/cm^2
Vertical 2ma/div
Horizontal 2v/div
Gate 0.5v/step

FIGURE 3-19 Drain Current Characteristics for Geometry No. 9, 100 Channel FET

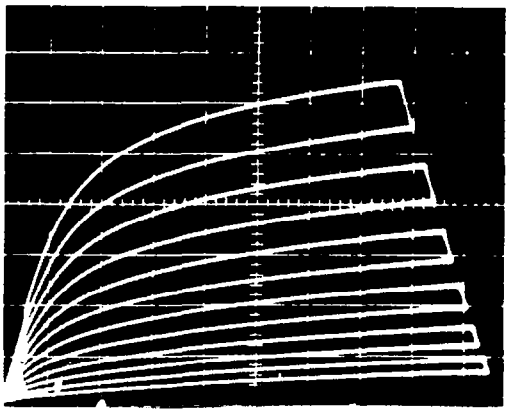

Pre Test
Vertical 5ma/div
Horizontal 2v/div
Gate 0.5v/step

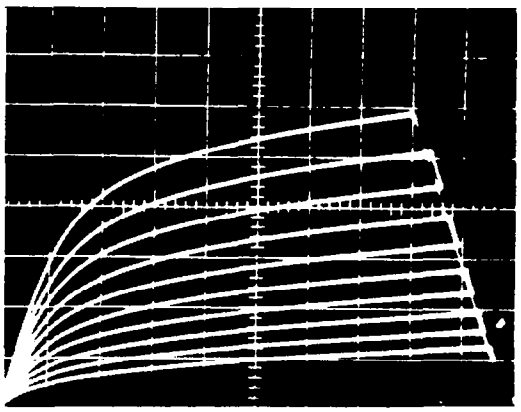

Integrated Flux 2.4×10^{13} protons/cm^2
Vertical 5ma/div
Horizontal 2v/div
Gate 0.5v/step

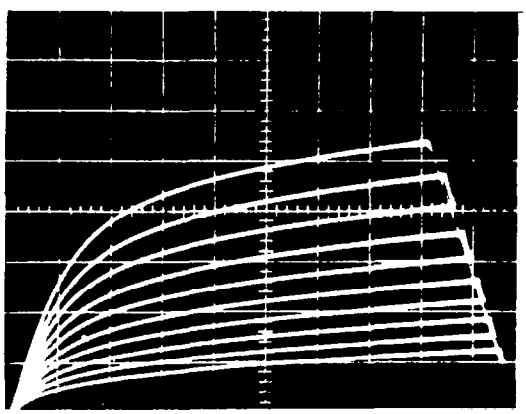

Integrated Flux 3.9×10^{13} protons/cm^2
Vertical 5ma/div
Horizontal 2v/div
Gate 0.5v/step

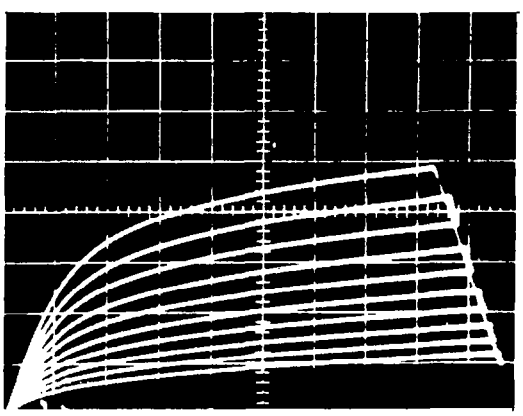

Integrated Flux 5.4×10^{13} protons/cm^2
Vertical 5ma/div
Horizontal 2v/div
Gate 0.5v/step

FIGURE 3-20 Drain Current Characteristics for Geometry No. 1, 380 Channel FET

geometry 11 was an initial experiment to look for the radiation effect and no other variations were irradiated at that time for comparison. To characterize the degradation of Geometries 9 and 1 the transconductance (g_m) was calculated at five gate voltages and four levels of integrated flux. These data are presented in Figures (3-21) and (3-22).

From an approximate solution of Poisson's equation for a cylindrical channel model the transconductance is a linear function of the density of free carriers.[9] The assumption of a linear carrier removal rate then leads to a linear decrease in g_m as observed.

In addition to these devices, a bulk sample of the channel material was irradiated to determine mobility changes by a Hall measurement. A significant drop and shift in peak of the current vs temperature plot for this sample was noted. After a five minute annealing at 200°C the pre-irradiation curve was recovered to within 5%. Similar recovery of pre-irradiation characteristics upon annealing was noted for the devices as well.

3.4.2 Comparison With Theory

Two facts stand out from an examination of the experimental data for the 2N708 discussed in the previous Section, and are of the utmost importance for the present investigation. These are, (a) the linear or near linear dependence of the common base current gain, α, on integrated flux, and, (b) the dependence of the slope of α as a function of integrated flux on the emitter current or injection level. The analysis to follow rests on these two experimental findings.

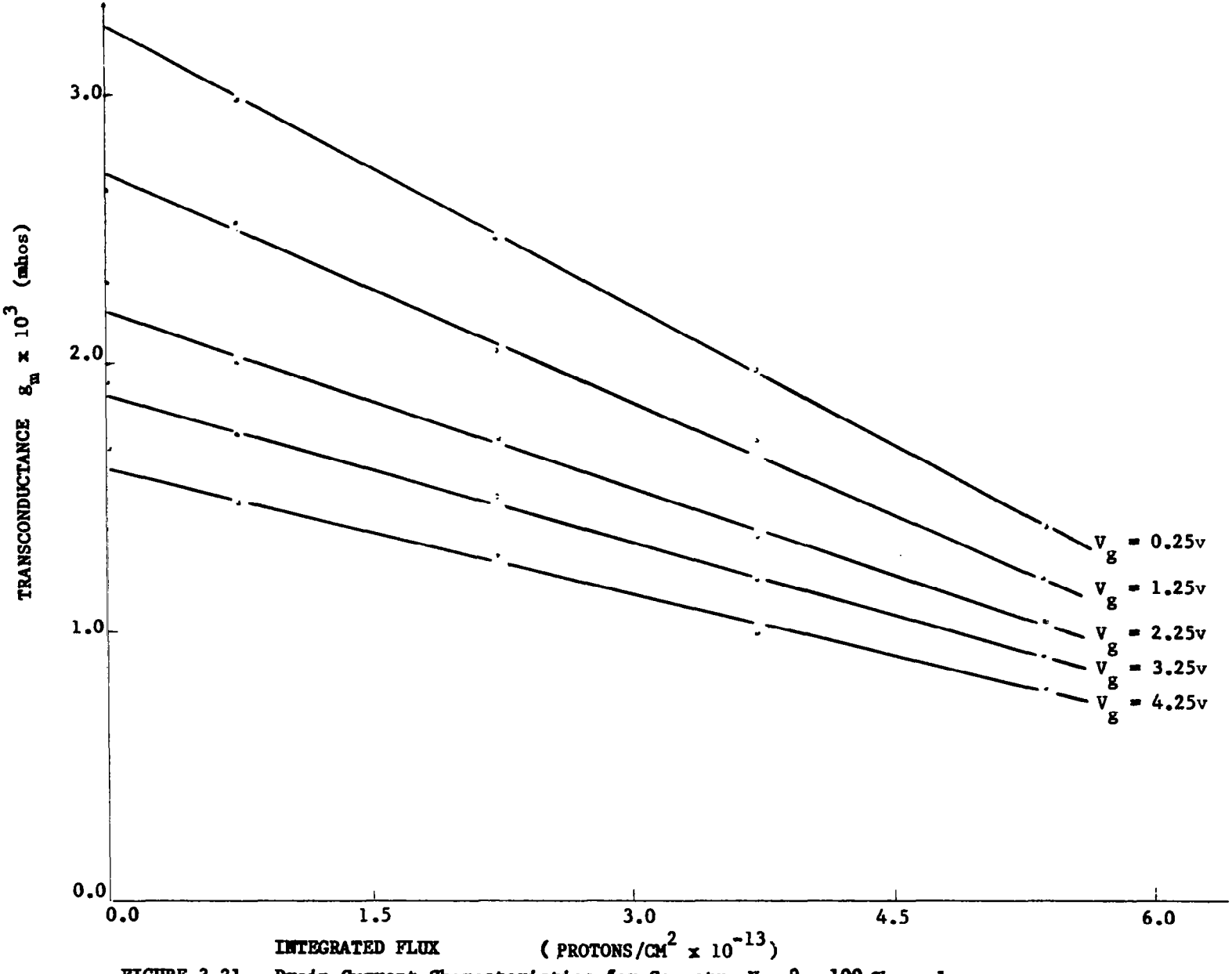

FIGURE 3-21 Drain Current Characteristics for Geometry No. 9, 100 Channels

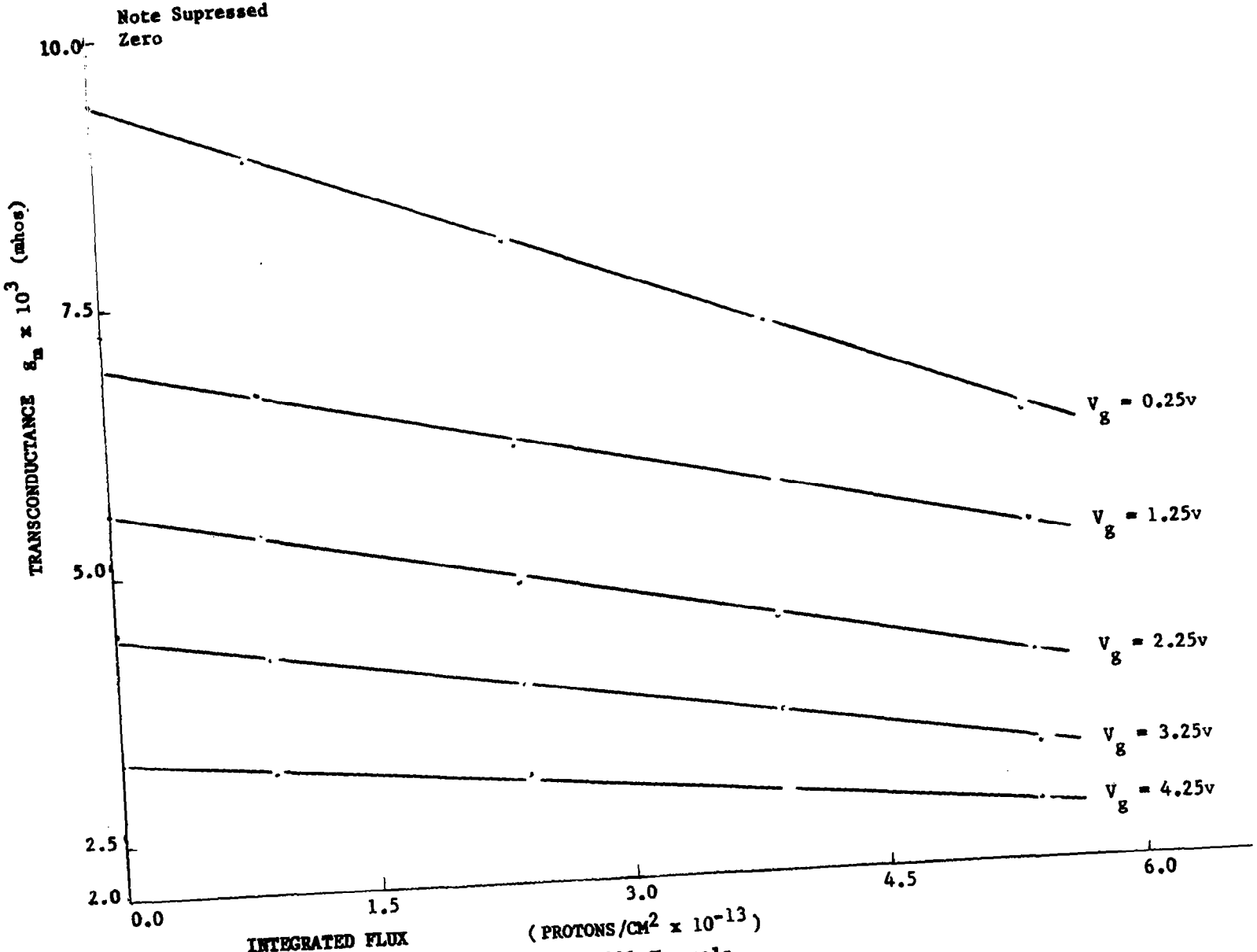

FIGURE 3-22 Degradation of Geometry No. 1, 380 Channels

The linear dependence, alone, of α on the integrated flux is explained most simply as follows. In Section 2.1 an expression was derived for α for the cylindrical model with non-zero surface recombination,

$$\alpha \cong \text{sech } (W/L)\left[1 + 2(2/\pi)^3 \ (sW^2/Dr_e) \right]^{-1} , \qquad (2.22)$$

with the approximation $(sW/D) << 1$; with the further approximations, $(W/r_e) << 1$, Equation (2.22) becomes,

$$\alpha \cong 1 - (1/2) \ (W/L)^2 - 2(2/\pi)^3 \ (sW^2/Dr_e) \qquad (2.24)$$

In essence, the model, as expressed in Equation (2.24) attributes the current gain α to the processes of volume recombination in the base and surface recombination in the emitter plane. With the substitution of the diffusion length degradation expression,

$$1/L^2 = 1/L_o^2 + K\varphi \ , \qquad (2.41)$$

Equation (2.24) becomes

$$\alpha(\varphi) = \alpha_o - (KW^2/2) \ \varphi \qquad (3.1)$$

where α_o is given by Equation (2.24) with L_o substituted for L. Equation (3.1) yields a linear dependence of α on flux φ. It will be noted that the surface term in Equation (2.24) enters only in the α_o term. The slope of α as a function of φ depends only upon the damage constant and the base width. The important point now is that while Equation (3.1) predicts a linear dependence of α on φ, it does not predict the observed dependence of

the slope on injection level and on design variables other than base width. It is clear that a generalization of Equation (3.1) is needed.

This generalization is provided by a consideration of high level injection effects and is discussed in Section 2.2 above. The results of the consideration are summarized in the expression for α, generalized to the case of high level injection, and are given in Equation (2.42),

$$\alpha(\varphi) = \alpha_o - KW^2 \left[(1 + Z/2)/(1 + Z)\right] F \left[Z, (\tau_o/\tau_\infty)\right] \varphi \qquad (2.42)$$

In contrast to Equation (3.1), the slope indicated in Equation (2.42), through the Z-parameter,

$$Z = I_{nE} W/qADN_a \quad , \qquad (2.39)$$

is now a function of the emitter current, I_{nE}, the base width, W (a double dependence), the emitter area, A, and the base doping level, N_a. In addition, the dependence on gold doping is probably represented by the material parameter, (τ_o/τ_∞). The agreement between Equation (2.42) and the results of experiment may now be checked in more detail.

The experimental data in all cases indicates a decreasing slope for increasing emitter current for the dependence of α on integrated flux φ, as shown, for example in Figure (3-8). Equation (2.42) is in accordance with this result since the slope, as determined by the factor $KW^2 \left[(1 + Z/2)/(1 + Z)\right] F$, is a decreasing function of Z (I_{nE}) for constant values of the other variations.

This is shown directly in Figure (2-2) for values of $(\tau_o/\tau_\infty) \gtrsim 1$. Similarly, Equation (2.42) predicts an increasing Z for decreasing emitter area A, and correspondingly a smaller slope for smaller emitter areas as observed experimentally in Figure (3-11). In addition, the base doping level, N_a, may be expected to vary with the emitter doping variation. Again, the data as shown in Figure (3-13) is in agreement with the prediction of Equation (2.42). In this case increased emitter doping represents increasing compensation of the base acceptor impurity, that is, a decreased N_a; which in turn implies an increasing Z and decreasing slope as predicted.

The above considerations, while they are qualitative in nature, indicate strongly that for the 2N708 the predominant radiation effect lies in diffusion length degradation in the base. This is inferred from the linearity of the data and follows from the inverse square dependence on diffusion length resulting from the volume recombination process. In addition, it may be concluded that injection level effects are important in the 2N708 at the lowest emitter current levels indicated, and that the inclusion of these effects will form a necessary part of an extended design effects program for the double diffused planar device.

4.0 DESIGN SPECIFICATIONS

On the basis of the results obtained from this program, definite design specifications can be enumerated for the 2N708 transistor which will lead to significant improvements in its radiation resistance. The physical design parameters which lead to the radiation resistant prototype 2N708 investigated in this program are listed in Table (3-2).

More important than these specific parameters for the 2N708 are the trends in design philosophy which should be applicable generally to the silicon planar configuration. Design specifications which summarize the results of the present program appear in Table (4-1). The following design trends, determined empirically or by comparison of theory and experiment, may be summarized as follows,

(1) Narrow base widths lead to significant improvements in radiation resistance.

(2) Small emitter radii reduce the rate of degradation of the current gain through the injection level effect.

(3) Reduction of base doping level also reduces degradation rate through the injection level effect.

(4) Czochralski material with its higher oxygen content is preferable to float zone material.

(5) The radiation resistance of a device is proportional to its gold concentration.

(6) Variations in the surface condition have little or no effect on the radiation resistance of the device. Standard HCl etching and dry-wet-dry SiO_2 surfaces are recommended to reduce leakage currents and maintain the best electrical performance.

Table 4-1

Specifications for Radiation Resistant Design

Processing Step	Geometrical Factors	Impurity Doping Concentrations	Surface Conditions
1. Crystal Selection		Czochralski material is better than Float zone material	
2. Lap and Polish			
3. Oxidized Epitaxial Growth		No correlation with epitaxial vs nonepitaxial material	
4. Base Photo Resist			
5. Base Diffusion and Oxidation	Narrow base widths 0.5 - 0.8μ are substantially better	Shallow Junction Diffusions ($< 2.0\mu$) with lower values of base conductivity are better	
6. Emitter Photo Resist	Small circular emitter geometries are better		
7. Emitter Diffusion and Oxidation	Shallow Junction Diffusions ($\approx 1.0\mu$) are more desirable	Shallow Junction Diffusions increase the emitter conductivity and maintain high emitter efficiency	No significant correlations with surface conditions were obtained. Standard HCl etch and dry-wet-dry SiO_2 surfaces are recommended.
8. Gold Evaporation and Diffusion		Highest gold concentrations compatible with the solid solubility of the doped crystal are best.	
9. Contacts, Headers, Bonding and Encapsulation			

No conclusions were reached on the subject of epitaxial versus non-epitaxial devices. Additional considerations, including double base diffusions, limitations in power handling in large geometry devices, and trade-offs with further desirable electrical characteristics, important for high frequency and switching applications, will be necessary in a more detailed design investigation.

5.0 REFERENCES

1. R. A. Schmeltzer, "Transient Characteristics of Alloy Junction Transistors Using a Generalized Charge Storage Model", New York Univ., Dept. of Elec. Eng.,Tech. Rept. 400-60, April,1962.

2. E. S. Rittner, Phys. Rev. 94, 1161 (1954).

3. G. C. Messenger and J. P. Spratt, Proc. IRE, 1038 (1958).

4. A. B. Phillips, Transistor Engineering, McGraw Hill, New York, 1962, p. 226, et seq.

5. G. C. Messenger, Nuclear Radiation Effects Conference, IEEE PGNS, Seattle, Washington, July, 1964.

6. W. M. Webster, Proc. IRE 42, 914 (1954).

7. W. Shockley and W. T. Read, Jr., Phys. Rev. 87, 835 (1952).

8. P. G. Hoel, Introduction to Mathematical Statistics, John Wiley and Sons, New York, 2nd Ed., 1954, p. 248.

9. R. P. Nanavati, An Introduction to Semiconductor Electronics, McGraw Hill, New York, 1963, p.386.

6.0 ACKNOWLEDGEMENTS

We would like to express our appreciation to Professor Charles Waddell of the University of Southern California for permission to use the proton linear accelerator. In addition, the help of Tom Inman, Earl White and their accelerator crews is gratefully acknowledged. Mr. Brian Gallagher and Mr. Jerry Mazenko of the Hughes Solid State Research Center provided necessary support in the fabrication of the transistors. Mr. Rainer Zuleeg provided the multichannel field effect transistors and aided in the interpretation of the data for these devices. Mr. Jim Allee provided guidance in statistical design. Mr. Daryl Butcher and Mr. Doug Gibson assisted in the design and development of the experimental instrumentation. Mr. Gene Scarlett assisted with the data reduction and was responsible for liaison with the computer group headed by Mr. Alan Bell.

7.0 APPENDIX

As shown in Section 2.1, the charge density distribution depends upon the solution of the following dual integral equations,

$$\int_0^\infty \varphi(p) J_o(rp) \left[\tanh\gamma W/(\gamma W+\lambda\tanh\gamma W)\right] dp = q_e \ , \ 0 \leq r < r_e \ , \tag{2.15}$$

$$\int_0^\infty \varphi(p) J_o(rp) dp = 0 \ , \ r_e < r < \infty \ . \tag{2.16}$$

For the special case of zero surface recombination velocity λ is zero and Equation (2.15) reduces to,

$$\int_0^\infty \varphi(p) \left[\tanh\gamma W/\gamma W\right] J_o(rp) dp = q_e \ . \tag{7.1}$$

The solution of Equations (2.16) and (7.1) is obtained by a method due to Tranter.* If it is assumed that

$$\varphi(p) = \sum_{m=o}^{\infty} a_m J_{2m+1}(r_e p) \ . \tag{7.2}$$

Equation (2.16) is automatically satisfied since

$$\int_0^\infty J_{2n+1}(r_e p) J_o(rp) dp = 0 \ , \ r_e < r < \infty \ . \tag{7.3}$$

The a_m must now be determined such that Equation (7.1) is satisfied. Tranter shows that this will be the case if the a_m obey the following iterative expression,

$$a_m = (2m+1) q_e r_e (kW/\tanh kW) \left[\delta_n - C_n + C_n' - C_n'' + \cdots\right] \tag{7.4}$$

* C. J. Tranter, Integral Transforms in Mathematical Physics, Metheum and Co., Ltd., 1959, p. 111

where

$$C_n = L_{o,n}\,, \qquad \delta_n = \begin{cases} 1, & n=o \\ o, & n>o \end{cases} \tag{7.5}$$

$$\left.\begin{aligned} C_n' &= \sum_{m=o}^{\infty} L_{m,n}\, C_m \\ C_n'' &= \sum_{m=o}^{\infty} L_{m,n}\, C_m', \quad \text{etc.} \end{aligned}\right\} \tag{7.6}$$

and $L_{m,n}$ is defined as follows,

$$L_{m,n} = (4n+2)\ (kW/\tanh kW) \int_o^{\infty} \left[(\tanh \gamma W/\gamma W) - (\tanh kW/kW)\right]\ J_{2m+1}\ (r_e p)$$
$$J_{2n+1}\ (r_e p)\ (dp/p) \tag{7.7}$$

Equation (7.7) is integrated by writing the hyperbolic function as a partial fraction expansion,

$$(1/p)\left\{(\tanh \gamma W/\gamma W) - (\tanh kW/kW)\right\} = -\,(2/W^2) \sum_{\ell=1}^{\infty} \frac{p}{(p^2+\mu_\ell^2)\mu_\ell^2}\,, \tag{7.8}$$

$$\text{where } \mu_\ell^2 = k^2 + (2\ell-1)^2\ \pi^2/4W^2 \tag{7.9}$$

Equation (7.7) with Equation (7.8) gives,

$$L_{m,n} = -(2/W^2)\ (4n+2)\ (kW/\tanh kW) \sum_{\ell=1}^{\infty} (1/\mu_\ell^2) \int_o^{\infty} \frac{p}{p^2+\mu_\ell^2}\ J_{2m+1}\ (r_e p)$$
$$J_{2n+1}\ (r_e p)\ dp \tag{7.10}$$

Carrying out the integration in Equation (7.10) gives,*

$$L_{m,n} = -(4n+2)/W^2 \quad (kW/\tanh kW) \quad (-1)^{m+n} \sum_{\ell=1}^{\infty} (1/\mu_\ell^2) \left[I_{2m+1}(r_e\mu_\ell) \; K_{2n+1} \right.$$

$$\left. (r_e\mu_\ell) + I_{2n+1}(r_e\mu_\ell) \quad K_{2m+1} \quad (r_e\mu_\ell) \right] \qquad (7.11)$$

It is now assumed that the base width, W, is much smaller than the radius of the emitter junction r_e. Then, from Equation (7.9)

$r_e\mu_\ell = \left[k^2 r_e^2 + (2\ell-1)^2 \pi^2 r_e^2/4W^2 \right]^{1/2} > (\pi r_e/2W) >> 1.$ The modified Bessel functions I and K in Equation (7.11) may be replaced by their asympototic values,**

$$I_\nu(z) \sim \left[e^z/(2\pi z)^{1/2} \right]$$

$$K_\nu(z) \sim (\pi/2z)^{1/2} \quad e^{-z}$$

and the bracketed expression in Equation (7.11) becomes $(1/r_e\mu_\ell)$.

Equation (7.11) becomes,

$$L_{m,n} \cong -(4n+2) \quad (kW/\tanh kW) \quad (-1)^{m+n} \quad (W/r_e) \sum_{\ell=0}^{\infty} \left[k^2W^2 + (2\ell-1)^2 \pi^2/4 \right]^{-3/2} \qquad (7.12)$$

* G.N. Watson, A Treatise on the Theory of Bessel Functions, 2nd Ed., Macmillan Co., New York, 1945, p. 429.

** Handbook of Mathematical Functions, Nat. Bur. Stand. App. Math. Ser. 55, 1964, p. 378.

For small values of (W/r_e), $L_{m,n}$ approaches zero and the iterative solution given by Equation (7.4) approaches,

$$\alpha_o \cong q_e r_e \ (kW/\tanh kW)$$
$$\alpha_m \cong o, \qquad m = 1, 2, \text{---} \tag{7.13}$$

The solution to the dual integral equations, therefore, for $(W/r_e) << 1$, is from Equation (7.2)

$$\varpi(p) \cong q_e \ (kW/\tanh kW) \ r_e J_1 (r_e p) \tag{7.14}$$

The minority carrier charge density in the base follows from Equations (2.13), and (2.14) of Section 2.0,

$$q(r,z) = r_e q_e \ (kW/\tanh kW) \int_o^\infty \left[\sinh\gamma(W-z)/\gamma W \cosh\gamma W\right] J_1(r_e p) J_o(rp)\,dp \tag{7.15}$$

for the case $(W/r_e) << 1$.